Applied Catalysis B: Environment and Energy 358 (2024) 124363

Contents lists available at ScienceDirect

Applied Catalysis B: Environment and Energy

journal homepage: www.elsevier.com/locate/apcatb

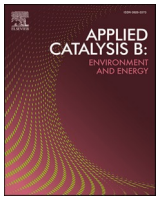

Pd loading threshold for an efficient noble metal use in Pd/CeO_2 methane oxidation catalysts

Deniz Zengel [a], Vasyl Marchuk [a], Merve Kurt [a], Florian Maurer [a], Agustin Salcedo [b], Carine Michel [b], David Loffreda [b], Mimoun Aouine [c], Stéphane Loridant [c], Philippe Vernoux [c], Heike Störmer [d], Maria Casapu [a,*], Jan-Dierk Grunwaldt [a,e,**]

[a] Institute for Chemical Technology and Polymer Chemistry (ITCP), Karlsruhe Institute of Technology (KIT), Kaiserstr. 12, Karlsruhe 76131, Germany
[b] CNRS, ENS de Lyon, LCH, UMR 5182,69342, Lyon cedex 07, France
[c] Université Claude Bernard-Lyon 1, CNRS, IRCELYON-UMR 5256, 2 av. A. Einstein, Villeurbanne Cedex F-69626, France
[d] Laboratory for Electron Microscopy (LEM), Karlsruhe Institute of Technology (KIT), Kaiserstr. 12, Karlsruhe 76131, Germany
[e] Institute of Catalysis Research and Technology (IKFT), Karlsruhe Institute of Technology (KIT), Hermann-von-Helmholtz-Platz 1, Eggenstein-Leopoldshafen 76344, Germany

ARTICLE INFO

Keywords:
methane oxidation
Pd catalyst activation and stabilization
in situ/operando spectroscopy
strong noble metal-support interaction
DFT modeling

ABSTRACT

The influence of the noble metal-support interaction on the performance, activation behavior and stability of Pd/CeO_2 catalysts for total methane oxidation was systematically investigated. A series of samples with 1–3 wt% Pd loading supported on CeO_2 with surface areas varying between 30 and 120 m^2/g were tested as-prepared and after different reductive treatments. Distinct Pd structural states were identified, which influence the catalytic performance depending on the pre-treatment and the theoretical monolayer Pd coverage of CeO_2. Although reductive treatments improved the catalytic activity, the stability strongly depended on the Pd coverage on ceria and the type of reducing agent. A threshold of Pd concentration on the ceria surface was identified that ensures optimal noble metal efficiency, activity and long-term durability. Below this threshold, rapid catalyst deactivation occurs due to redispersion on the strongly interacting support whereas above this threshold Pd is prone to sintering irrespective of the atmosphere.

1. Introduction

Due to their unique properties, noble metal catalysts are widely used for the production of various chemicals and in emission control. However, their ever-increasing global demand is challenged by the high costs and limited availability of resources. Additionally, noble metal-based catalysts are susceptible to aging and poisoning processes. Such phenomena are countered in numerous cases by the use of considerable amounts of precious metals, which results in highly expensive catalytic converters. Considering the still limited recycling rates [1], this strategy is no longer acceptable in the long term, and the efficient use of the precious metal components is compulsory in future catalyst formulations.

An important example are the noble metal-based catalysts used for the removal of hydrocarbon emissions in the exhaust of biomethane/natural gas engines. During the transition towards fully renewable energy sources, methane combustion is regarded as an advantageous path for energy production, especially considering the lower CO_2 emissions compared to those resulting from the combustion of traditional liquid fuels [2]. This technology requires the catalytic removal of the CH_4 slip due to its 20 times higher greenhouse potential in comparison to CO_2. For lean combustion engines, Pd-based catalysts are known to outperform other catalyst formulations. Typically, substantial noble metal (NM) loadings are used on supports such as Al_2O_3 or CeO_2-ZrO_2 to ensure low light-off temperatures and good catalyst durability [2–5]. In spite of this, water inhibition and sulfur poisoning still affect the methane oxidation activity considerably. Whereas the first process is a result of hydroxyl group formation on the surface of Pd particles, sulfur poisoning affects both the active species and the carrier material [6,7]. For catalyst regeneration, reductive treatments can be periodically

* Corresponding author.
** Corresponding author at: Institute for Chemical Technology and Polymer Chemistry (ITCP), Karlsruhe Institute of Technology (KIT), Kaiserstr. 12, Karlsruhe 76131, Germany
E-mail addresses: maria.casapu@kit.edu (M. Casapu), grunwaldt@kit.edu (J.-D. Grunwaldt).

https://doi.org/10.1016/j.apcatb.2024.124363
Received 19 February 2024; Received in revised form 4 June 2024; Accepted 1 July 2024
Available online 2 July 2024
0926-3373/© 2024 The Authors. Published by Elsevier B.V. This is an open access article under the CC BY license (http://creativecommons.org/licenses/by/4.0/).

applied, either around catalyst operating temperatures to recover the activity upon water inhibition or at high temperatures for removal of sulfur species [2,8,9]. Despite partial or complete regain in activity, in the long term such treatments lead also to noble metal sintering, which is an irreversible deactivation process on weakly interacting supports [10]. In contrast, on ceria-based materials the *in situ* tuning of the noble metal particle to the optimal size is potentially possible [11]. In a first step, a highly dispersed state can be generated under oxidizing conditions at high temperatures due to the strong noble metal-support interaction. Here the ceria surface area plays an important role since the formation of single sites or small clusters requires the formation of NM-CeO_2 bonds for most of the noble metal atoms [12,13]. In a next step, a pre-reduction treatment can be applied at specific temperatures to obtain the optimal noble metal particle size. This concept has been successfully demonstrated for Pt/CeO_2 oxidation catalysts during CO oxidation [11,14]. In contrast, the role of noble metal – support interplay has been insufficiently evaluated for Pd/CeO_2 methane oxidation catalysts. Furthermore, for such high temperature reactions obtaining an outstanding catalytic activity at low temperatures by tuning the noble metal particle size is relevant only if this state is preserved over the entire temperature range of methane oxidation, bearing in mind the increased noble metal redispersion rate at elevated temperatures.

In this study, the influence of ceria specific surface area, pre-treatment procedure and noble metal loading on the activity and stability of Pd/CeO_2 catalysts is thoroughly investigated. The effect of the initial noble metal state is addressed by careful variation of the noble metal concentration on the ceria surface from below to above the theoretical monolayer coverage. The evolution of the obtained catalyst series with different surface noble metal concentrations (SNMC) is analysed by complementary *ex situ and in situ/operando* characterization methods including X-ray diffraction (XRD), Raman spectroscopy, diffuse reflectance infrared Fourier transform spectroscopy (DRIFTS), electron microscopy and X-ray absorption spectroscopy (XAS). In order to elucidate the nature of the adsorption sites on the catalyst surface, the DRIFTS experimental results are compared to those obtained by density functional theory (DFT) calculations.

2. Experimental section

2.1. Catalyst preparation

A series of Pd/CeO_2 catalysts with noble metal loadings between 1.0 and 3.0 wt% were prepared *via* incipient wetness impregnation (IWI). Before the impregnation step, the CeO_2 support (SOLVAY) was calcined at 700 °C for 5 h in static air, leading to a BET surface area of 120 m^2/g and a pore volume of 0.28 mL/g. Next, an aqueous solution of tetraamine palladium (II) nitrate (Pd 5.0 wt%, 99.9 % purity, abcr) was added dropwise, and the catalyst powder was homogenized in a mortar afterwards. The obtained samples were dried for 12 h at 80 °C and calcined subsequently at 500 °C for 5 h in static air. These samples are denoted xPd/CeO_2-120 (with x being the Pd wt% loading). Three additional samples with 2 and 3 wt% Pd loading were supported on low surface area CeO_2 (60 m^2/g and 30 $m^{2/}g$), and were denoted accordingly as xPd/CeO_2-60 and xPd/CeO_2-30, respectively. Whereas the CeO_2-60 support was obtained by calcining the high surface area CeO_2 at 900 °C for 10 h, CeO_2-30 was obtained as described in [15]. Unless stated otherwise, all catalysts were calcined for 10 h at 800 °C in static air (degreening step) to disperse the noble metal homogenously over the CeO_2 surface, in a procedure similar to that reported by Maurer et al. [13].

2.2. Characterization methods

The noble metal loading of the as prepared samples was verified by inductively coupled plasma optical emission spectrometry (ICP-OES) using an OPTIMA 4300 DV spectrometer (PerkinElmer) at the Institute for Applied Materials - Applied Materials Physics (IAM-AWP, KIT). In general, only a minor deviation was found for Pd concentrations in the differently loaded samples in comparison to the aimed values (Table S1).

Powder X-ray diffraction measurements were performed using a Bruker D8-Advance diffractometer with Cu Kα radiation over a 2θ range of 20–120° with a step size of 0.017°. The Inorganic Crystal Structure Database (ICSD) was used for phase identification.

A Belsorp Mini II (Bel Japan Inc.) instrument was used to determine the surface area and the pore volume of the catalyst samples. Approximately 80 mg of sample were degassed at 300 °C under vacuum for 2 h. Afterwards, the adsorption and desorption of N_2 were measured and evaluated with the Belsorp Adsorption/Desorption Data Analysis Software using the Brunauer-Emmet-Teller (BET) isotherm [16].

Raman spectroscopy was performed with an inVia Raman spectrometer (Renishaw) equipped with a frequency doubled Nd:YAG laser (532 nm, ~100 mW at the source) and a Leica DM2500 optical microscope. 0.1 % of laser power was employed together with a 2400 lines/mm grating. Spectra were recorded from 5 different points with an acquisition time of either 60 s or 180 s in the spectral range of 60–1300 cm^{-1}. All obtained spectra for each sample were averaged. The software WiRE 4.2 (Renishaw) was used for the data treatment. Each spectrum was noise filtered and averaged after cosmic ray removal.

High annular angle dark field scanning transmission electron microscopy (HAADF-STEM) imaging and energy dispersive X-ray spectroscopy (EDXS) mapping were performed at the Laboratory for Electron Microscopy (LEM, KIT) using an FEI OSIRIS (FEI, Eindhoven, The Netherlands) microscope operated at 200 kV. Prior to the electron microscopy measurements, the samples were pre-treated to match specific stages of the testing procedure. For each sample, a particle size distribution analysis was conducted with the ImageJ software, by evaluating up to ~950 particles. Both the size distribution maximum and the full width at half maximum (FWHM) were determined by means of a Gauss fit of the counted particles. A FEI TITAN ETEM G2 80–300 kV instrument equipped with an objective Cs aberration corrector was used for STEM-EDX mapping on 3.0 wt% Pd/CeO2–120. The sample was crushed and dispersed in ethanol using ultrasonication, deposited onto a holey carbon-coated 200 mesh Cu grid, and dried under a lamp. To avoid potential contamination during analysis and eliminate any remaining carbon residues, the sample was cleaned for 20 s in an Ar/O_2 plasma cleaning process (Plasma Prep 5, GaLa Instrument). The catalyst was *in situ* reduced in the ETEM at 500 °C for 2 h in 18 mbar H_2 or oxidized for 10 min in 10 mbar O_2 at 300 °C, 500 °C and 800 °C. After each oxidation step, the sample was rapidly cooled down in high vacuum to room temperature for performing EDX mappings.

In situ diffuse reflectance infrared Fourier transform spectroscopy (DRIFTS) measurements were performed during CO adsorption experiments using a Bruker VERTEX 70 FTIR spectrometer equipped with diffuse reflectance optics (Praying Mantis, Harrick Scientific Products) and a high temperature *in situ* cell (Harrick Scientific Products). As detector, a mercury cadmium telluride detector cooled with liquid nitrogen was used. A thermocouple-controlled heating cartridge (HTRS-26, Quantum Design) was employed to change the temperature of the sample crucible. To obtain a deeper penetration of the incident beam and, thus, increase the contribution of the diffusely reflected infrared radiation into the spectrum, 50 mg of the Pt/CeO_2 catalysts were diluted to a total of 1 g material using a non-absorbing CaF_2 reference. After dilution, the samples were pressed and sieved to a particle size between 100 and 200 μm. Approximately 50 mg of catalyst-CaF_2 mixture was used for the measurements. In a first step the sample surface was cleaned in 100 mL/min Ar at 250 °C for 1 hour. To study the CO adsorption, a gas mixture containing 1000 ppm CO/Ar was applied at a total flow rate of 100 mL/min. The resulting gas mixture at the cell outlet was monitored using a mass spectrometer (OmniStarTM, Pfeiffer Vacuum). Prior to the start of measurement, a background spectrum of the cleaned catalyst sample was recorded in Ar at 30 °C. For the background spectrum as well as the CO adsorption spectrum under reaction conditions, 200 scans

were collected, which were then automatically averaged and processed as one spectrum over a wavenumber range of 400–4000 cm^{-1}. The spectra obtained were evaluated using the Kubelka-Munk function.

Operando X-ray absorption spectroscopy (XAS) measurements were conducted for the 2.0 wt% Pd/CeO_2 catalyst. XAS data at the Pd K-edge were acquired at the SAMBA beamline of the SOLEIL synchrotron (France). For all experiments about 7.5 mg sample (sieved fraction: 100–200 μm) were located in a quartz glass capillary (1.5 mm inner diameter, 10 μm wall thickness) and heated by an air blower (FMB Oxford). A similar experimental procedure, including catalyst pre-treatment and light-off/light-out cycles, as the one applied during the catalytic activity experiments was used. Gases were dosed by mass-flow controllers (Bronkhorst) with a total gas flow of 50 mL/min, resulting in catalyst weight hour gas space velocity (WHSV) of 20000 $L{\cdot}g_{NM}^{-1}{\cdot}h^{-1}$. XANES spectra were continuously recorded during heating/cooling of the catalyst bed with a ramp rate of 10 °C/min under reducing conditions (2.0 % H_2/0.5 % CO in He) or reaction gas mixture (3200 ppm CH_4, 10 % O_2 in He). EXAFS spectra were collected around room temperature after different treatment steps. The obtained XAS data were analyzed with the ATHENA software package. [17]

2.3. Catalytic tests

A sieved catalyst powder (125 – 250 μm) diluted with quartz sand (SiO_2) was used for the catalytic tests in a plug-flow quartz glass reactor (inner diameter of 0.8 cm). The catalyst bed was fixed with quartz wool and built in a test bench of the Emission Control Center Karlsruhe. For the tests of the 1.0 wt% Pd/CeO_2 catalyst, 300 mg of sample were diluted with 700 mg of quartz sand. For the other samples in this study, the amount of catalyst in the reactor was adjusted to maintain the same noble metal weight hourly space velocity throughout all measurements. The applied gas mixtures were generated with mass flow controllers (MFC, Bronkhorst). Generally, the following pre-treatment procedures were used: (i) degreening treatment for 1 h at 800 °C in 10 % O_2/N_2; (ii) reductive treatment at 250 – 500 °C for 2–60 min in 0.5 % CO / N_2 or in 2 % H_2 / N_2. For determining optimal pretreatment parameters, some samples were calcined for 1 h at 550 °C in 10 % O_2 / N_2 and tested without further reduction. All catalytic tests were conducted in a gas mixture containing 3200 ppm CH_4, 0–5 % H_2O, 10 % O_2 in N_2. The gas flow was varied to obtain a noble metal weight hourly space velocity of 6600 $L{\cdot}g_{NM}^{-1}{\cdot}h^{-1}$ (low WHSV) or of 20000 $L{\cdot}g_{NM}^{-1}{\cdot}h^{-1}$ (high WHSV). The gas composition was determined using a Multigas™ 2030 FTIR Continuous Gas Analyzer from MKS Instruments. A typical test procedure included a degreening step at 800 °C in oxidizing conditions followed by light-off/light-off activity measurements (1–3 L_{Off}/L_{Out} cycles) between 200 and 550 °C at a ramping rate of 5 °C/min (cf. illustration in Fig. S23 in the supporting information). After determining the initial activity, the catalyst was activated under reductive conditions at 250–500 °C for 1–60 min. Three light-off/light-out cycles were afterwards conducted in reaction mixture. Rates of methane oxidation were calculated at 300 °C from Arrhenius diagrams based on temperature values for four conversion points below 20 % (see p. S13 of the SI, Fig. S16, tables S4-S12 for the details).

2.4. Density functional theory calculations

Density functional theory calculations were performed using the VASP code.[18,19] The exchange-correlation energy was calculated under the generalized gradient approximation (GGA), with the Perdew–Burke–Ernzerhof (PBE) functional.[20] The long-range dispersion DFT-D3(BJ) correction was used.[21,22] The valence electrons were treated on a plane-wave basis with an energy cut-off of 400 eV, whereas the core electrons were represented with the projector-augmented wave (PAW) method.[23,24] Total energies were calculated with a numeric precision of 10^{-6} eV. The DFT+U approach was implemented with Dudarev's scheme,[25] to consider strong electronic correlation effects due to charge localization and compensate for the self-interaction error, [26–30] with U_{eff} of Ce(4 f) set to 4.5 eV.[31,32] The forces were converged to ±0.02 eV/Å.

Harmonic vibrational frequencies were obtained by diagonalization of the Hessian matrix, deriving the force constants from finite differences with atomic displacements of 0.02 Å in the positions of CO molecules. Anharmonic corrections were introduced by fitting the potential energy around the equilibrium state in the space of the normal coordinates to a third-order development of the Morse potential. In addition, all frequencies have been scaled by a factor of 1.0224, chosen so that the calculated stretching frequency of gas-phase CO matches the experimental value (2143 cm^{-1}).

3. Results and discussion

3.1. Deactivation effects occurring in Pd/CeO_2 catalysts

To evaluate the different deactivation paths of ceria-based samples, light-off/light-out catalytic cycles were conducted in a first step for the 2 wt% Pd samples supported on low surface area ceria (2 Pd/CeO_2-30) and high surface are ceria (2 Pd/CeO_2-120). Fig. 1a shows that without any pre-treatment the catalyst containing 2 wt% Pd on a low surface CeO_2 (~30 m^2/g) exhibits a T_{50} temperature (50 % CH_4 conversion) of 333 °C and full conversion of CH_4 at 460 °C in a gas mixture containing 3200 ppm CH_4, 10 % O_2 in N_2 at a weight hourly space velocity of 6600 $L{\cdot}g_{NM}^{-1}{\cdot}h^{-1}$. Only a slight decrease in the methane oxidation activity is observed over two consecutive light-off/light-out cycles. Previous studies have shown similar activity trends for Pd/Al_2O_3 catalysts [15, 33], and the observed decrease in activity was assigned to an inhibition effect caused by the water formed during the reaction that blocks the catalyst surface.

After increasing the gas flow to reach a WHSV of 20000 $L{\cdot}g_{NM}^{-1}{\cdot}h^{-1}$, a shift of the CH_4 conversion towards higher temperatures is observed (T_{50} at 369 °C), with complete oxidation only being achieved at 550 °C. Also in this case a relatively good stability is noticed during a 2nd methane oxidation cycle for the 2 wt% Pd/CeO_2-30 catalyst, with only a minor decrease of the activity at low temperatures.

For the same high gas flow but with the noble metal supported on a high surface area CeO_2 (120 m^2/g), a 2 wt% Pd/CeO_2-120 catalyst shows a very poor performance, with only 30 % methane conversion measured at 550 °C (Fig. 1b). Despite the use of high surface area and thermally stable supports is a favoured path in heterogeneous catalysis, this contrasting result is most likely due to the different distribution of Pd species on the high surface area ceria. Such an effect is in line with recently reported results for various oxidation reactions over single sites or small noble metal clusters supported on ceria [13,34]. Although we cannot exclude that the water inhibition affects particles with different dispersion in a distinct manner, the onset of methane oxidation in a dry atmosphere after a prior catalyst thermal treatment at 550 °C is strictly affected by the catalyst structure.

Taking into account the pronounced impact of the support specific surface area on the catalyst performance for the same noble metal loading, i.e. different surface noble metal concentrations, this study aims at exploiting this peculiarity for providing the optimal activity and stability for Pd/CeO_2 during methane oxidation. For this purpose, a series of Pd/CeO_2 catalysts containing different noble metal loadings on ceria supports with surface areas between 30 and 120 m^2/g was prepared, and exposed to various degreening and pre-treatment procedures prior to the catalytic tests, as described in the following.

3.2. Effect of noble metal dispersion and pretreatment conditions on methane oxidation activity

At first, the 2 wt% $PdCeO_2$-120 catalyst was thermally treated at 800 °C for 10 h in oxidizing atmosphere, which is expected to induce redispersion of the noble metal particles due to the strong interaction

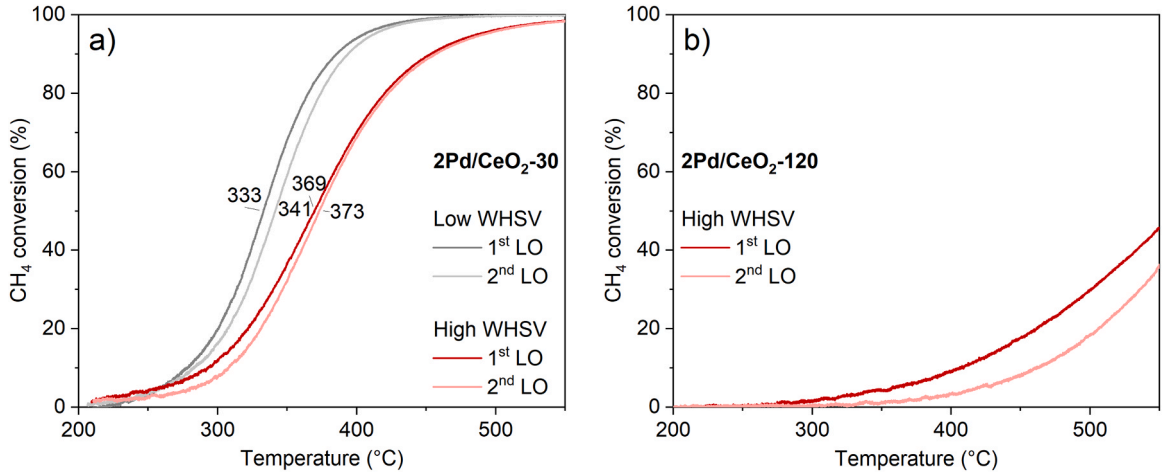

Fig. 1. Conversion of methane by total oxidation over 2 wt% Pd/CeO_2 catalysts supported on low surface area (a) and high surface area (b) CeO_2. Gas mixture: 3200 ppm CH_4, 10 vol% O_2 in N_2 at a weight hourly space velocity of 6600 $L \cdot g_{NM}^{-1} \cdot h^{-1}$ (low WHSV) and 20000 $L \cdot g_{NM}^{-1} \cdot h^{-1}$ (high WHSV). The samples were tested after thermal treatment at 550 °C in 10 % O_2 / N_2 without further reduction.

between Pd and ceria. As illustrated in Fig. 2a, after the high temperature treatment Pd is present as sub-nanometer entities in the HAADF-STEM images and the EDXS maps of the noble metal distribution on ceria surface. Despite PdO has been ascribed in previous studies as the active species for methane oxidation [33,35,36], the resulting noble metal state in the 800°C-degreened sample does not seem to be able to activate the C-H bond of CH_4. Only about 10 % CH_4 conversion is observed at 550 °C over the 2 wt% Pd/CeO_2-120 catalyst (Fig. 2d), which is even lower than the activity of the as prepared sample (calcined at 500°C, Fig. 1b). This outcome is in contrast to the DFT study of Su et al. [37], who proposed a highly active state and a lower activation barrier for CH_4 dissociation on the surface of a Pd-CeO_2(111) solid solution containing two Pd^{2+} ions substituting one Ce^{4+} in comparison to bulk PdO. On the other side, a similar result was reported recently by Jiang et al. [34] for a 1 wt% Pd/CeO_2 catalyst after calcination at 800 °C.

A high CH_4 oxidation activity was measured for this catalyst only after reduction in 2 % H_2/N_2 (Fig. 2e). Additionally, our results show that the stability of the induced catalyst state is highly dependent on the applied pre-treatment conditions. Despite a significant activity gain was obtained upon reduction at 350 °C for 1 h (T_{50} at 290 °C, Fig. S1 a), the methane conversion drops already during heating to 550 °C under reaction conditions. Analogous, shorter reduction treatments even at higher temperatures led only to a minor gain in activity and fast catalyst deactivation (Fig. S2). Only by applying the H_2-reductive atmosphere for 1 h at 500 °C, the resulting methane oxidation activity is maintained

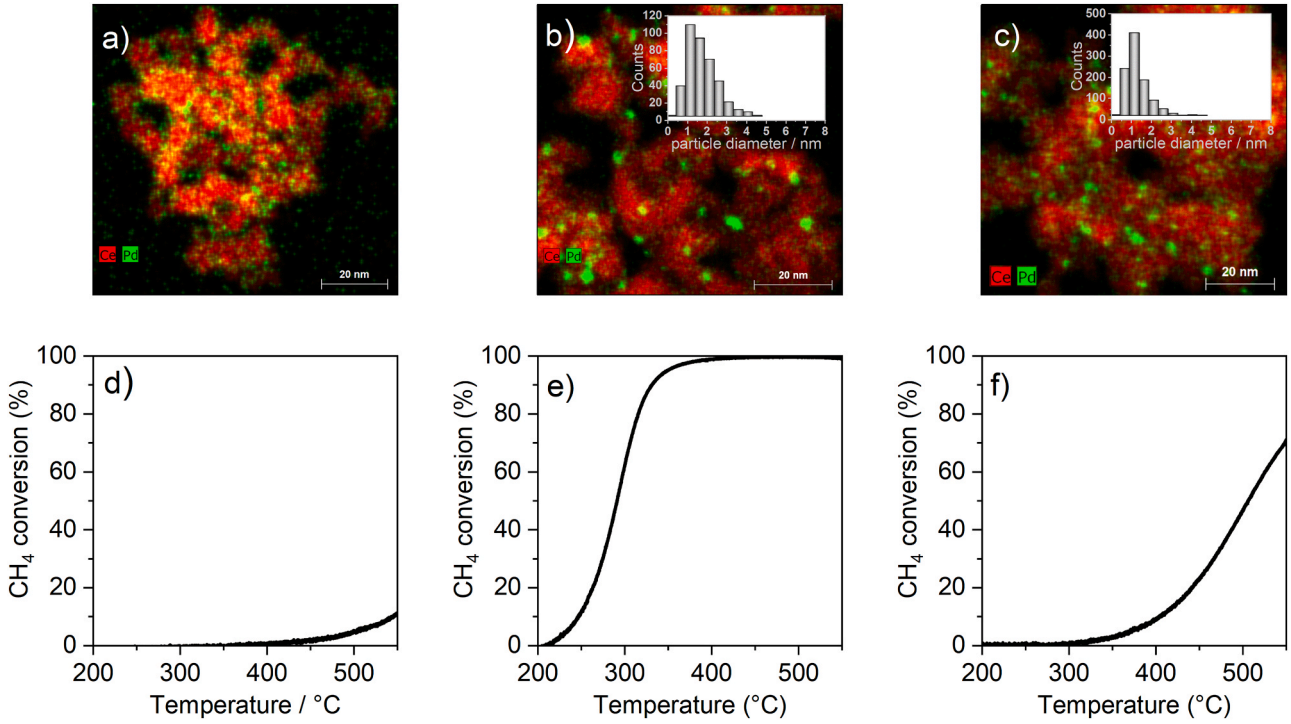

Fig. 2. STEM-EDX maps of 2 wt% Pd/CeO_2-120 catalyst after thermal treatment at 800 °C (a), H_2 reduction at 500 °C for 1 h (b) and at the end of 3 light-off/light-out cycles (c). The corresponding CH_4 conversion during the 1st light-off for the catalyst treated at 800 °C (d), H_2-reduced at 500 °C (e), and the 3rd light-off after the H_2-reductive pre-treatment (f). Gas mixture: 3200 ppm CH_4, 10 vol% O_2 in N_2 at a weight hourly space velocity of 20000 $L \cdot g_{NM}^{-1} \cdot h^{-1}$.

over the entire temperature range besides reaching 50 % conversion at 283 °C and full conversion at 375 °C (Fig. 2e). The improvement in activity due to catalyst pre-reduction was previously assigned by Lott et al. [33] to formation of larger and reduced Pd particles on alumina and ceria, which are less prone to H_2O inhibition in comparison to PdO_x nanoparticles. A similar trend was reported by Stakheev et al. [38] for a series of Pd/Al_2O_3 catalysts, which showed an almost linear relation between the methane oxidation activity and the increase of Pd particle size. Sintering of Pd species to nanoparticles of an average size of 1.7 nm (size distribution between 1 – 5 nm) was found after hydrogen reduction of the 2 wt% Pd/CeO_2-120 catalyst at 500 °C (Fig. 2b). Nonetheless, also in this case, after a first light-off/light-out cycle to 550 °C a pronounced drop in activity was measured, with an increase in T_{50} from 290 °C to 475 °C. During the 3rd catalytic cycle (Fig. 2f) the T_{50} increased only slightly to 505 °C, indicating a certain catalyst stabilization.

Generally, a decrease in the catalytic activity is observed for most Pd-based methane oxidation catalysts irrespective of the formulation during consecutive light-off/light-out cycles in dry atmosphere [2]. This behaviour has been attributed so far to the water inhibition/deactivation effect due to formation of hydroxyl groups on Pd and support surface, which block the active species at low temperature [3, 39]. To counterbalance this effect, the use of supports with increased oxygen mobility is known to be beneficial for improving the water tolerance [40]. Nonetheless, the water deactivation effect is not absent for ceria supported catalysts, and is expected to affect Pd species during our tests. However, the pronounced drop in the catalytic activity as observed in this study must be caused by additional catalyst structural changes. As shown by the electron microscopy investigations of the 2 wt % Pd/CeO_2-120 catalyst after the three light-off/light-out cycles, partial redispersion of Pd particles occurs leading to an average size of 1.2 nm (Fig. 2c). As it has been previously noticed for similar noble metal – ceria systems [12], this pronounced instability of the pre-reduced 2 wt% Pd/CeO_2-120 catalyst in oxygen rich atmosphere is most probably endorsed not only by catalyst exposure to high temperatures but also by the high surface area of the ceria carrier (120 m^2/g) used in this study. Considering that a moderate drop in Pd particle size was identified between the reduced and the post-reaction catalyst state, the major diminishment in activity must be linked to the high structure sensitivity of CH_4 oxidation on small Pd nanoparticles, which appear much more frequently in the EDX map (Fig. 1c) after the third light-off compared to the freshly reduced sample [36]. Such phenomena are additionally emphasized by the high gas hourly space velocity applied in this study.

A similar activity improvement was obtained if CO was used as reducing agent (Fig. 3a) instead of H_2. Both reducing gases as well as other hydrocarbons are expected to be present under stoichiometric or fuel-rich conditions [41], which could be used for catalyst regeneration

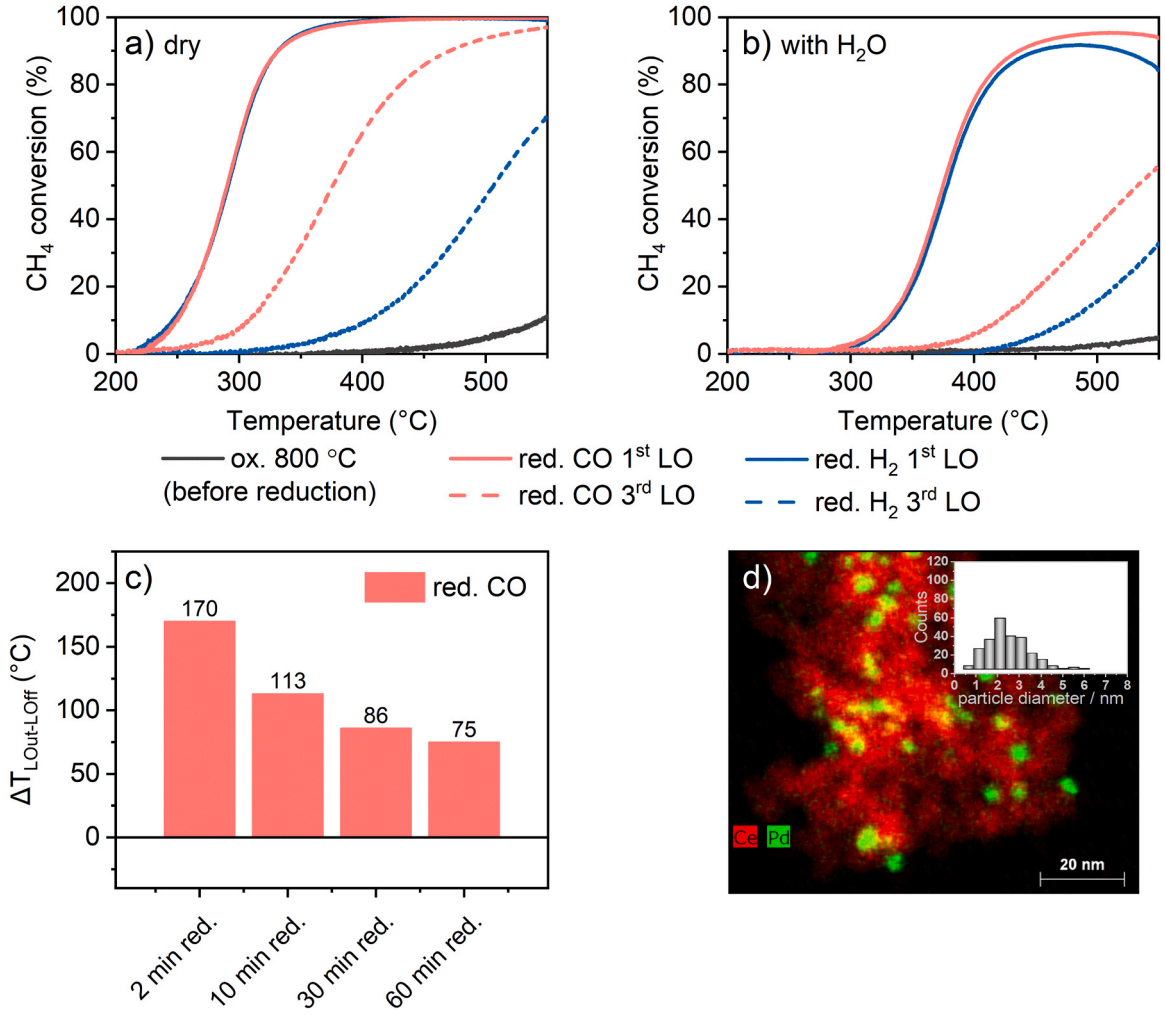

Fig. 3. Conversion of methane by total oxidation during 3 consecutive light-offs for 2 wt% Pd/CeO_2-120 catalyst after thermal treatment at 800 °C and reduction in 2 % H_2/N_2 (red. H_2, blue) or 0.5 % CO/N_2 (red. CO, red) for 1 h at 500 °C. Gas mixture: (a) 3200 ppm CH_4, 10 vol% O_2 in N_2; (b) 3200 ppm CH_4, 5 vol% H_2O, 10 vol % O_2 in N_2 at a weight hourly space velocity of 20000 $L \cdot g_{NM}^{-1} \cdot h^{-1}$. (c) Differences between the light-off (T_{LOff}) and light-out (T_{LOff}) temperatures of 50 % CH_4 conversion in dry reaction conditions after calcination at 800 °C and CO reduction for 2–60 min at 500 °C. (d) HAADF-STEM EDX map of 2 wt% Pd/CeO_2-120 catalyst after CO reduction at 500 °C for 1 h.

or activation during real operation. As illustrated in Fig. 3, upon reduction for 1 h at 500 °C in 0.5 % CO / N_2 an almost identical increase in CH_4 conversion was observed during the 1st light-off in activity. T_{50} values of 246 °C and 249 °C were recorded after catalyst activation in H_2 and CO, respectively. On the other hand, a significantly less pronounced catalyst deactivation was observed during the following activity cycles for the catalyst reduced with CO. Thus, an increase of the temperature for 50 % CH_4 conversion to 291 °C was measured during the 2nd light-off cycle. During the 3rd light-off cycle the activity varied only slightly (T_{50} at 307 °C), further confirming the improved catalyst stability. Considering that CO is also expected to reduce the noble metal species to metallic state, this improvement in catalyst stability could be caused by the formation of larger Pd particles that are more stable towards high temperature redispersion. The CO-assisted migration and growth of Pd particles due to formation of Pd-carbonyl species has been previously suggested in the literature on SiO_2 [42] and Fe_3O_4 [43]. Recently, CO was reported to drive the migration of Pd atoms on ceria even at room temperature [34]. In a study on the effect of H_2 and CO reducing agents on the state of Pd in a Pd/SSZ-13 NO_x adsorber catalyst, significantly larger particles were formed during CO reduction at 500 °C in comparison with those obtained after H_2-reduction [44]. A pronounced dependency of the CO oxidation activity on the reducing agent was found for Pt/CeO_2-based catalysts by Gänzler et al. [14], with CO showing the highest reduction efficiency of the noble metal and ceria support in comparison to C_3H_6 and H_2. In fact, the EDXS elemental mapping images obtained for the CO-reduced catalyst (Fig. 3d) shows that slightly larger particles are formed in the presence of CO in comparison to the catalyst pre-treated in H_2 (Fig. 2b). An average particle size of 2.5 nm was measured and a size distribution between 1 and 7 nm, which is overall with 1–1.5 nm larger than that obtained after reduction in hydrogen. Although the difference in the measured size is not major, it helps to rationalize the higher stability observed during the catalytic tests.

Analogously to the activation by a H_2 reduction pre-treatment, the catalyst was also probed after CO exposure at different temperatures as alternative reduction procedures. Also in this case an activation was found but a good stability during the first CH_4 oxidation light-off was only obtained at pre-treatment temperatures above 350 °C (details, cf. Fig. S1 b). At lower activation temperatures a clear diminishment in activity was observed above 450 °C, most probably caused by Pd nanoparticle redispersion. Almost the same T_{50} temperatures were obtained for the 2 wt% Pd/CeO_2-120 catalyst after CO reduction between 1 and 30 min at 500 °C (Fig. S3). However, the activity drops already during the first light-off/light-out cycle, in direct correlation with the lower reduction time. The faster deactivation is indicated also by the larger difference between the light-off and light-out temperatures of 50 % conversion (Fig. 3c) that was measured for the shorter activation steps. Whereas this difference amounts to about 75 °C after reduction for 1 h at 500 °C, the light-out temperature is with 170 °C higher after 2 min CO reduction. The direct correlation between the decrease in activity and noble metal redispersion is supported by the HAADF-STEM EDXS images collected for the 2 wt% Pd/CeO_2-120 catalysts after 1 h reduction in 0.5 % CO/N_2 (Fig. S4a) and after three consecutive light-off/light-out methane oxidation cycles (Fig. S4b). Overall, comparable catalyst stability is obtained on this high surface area support only if over 30 min reduction periods are applied. To better identify the catalyst structural changes and their relationships with the obtained activity and stability, further investigations were conducted mostly for the catalysts reduced for 1 h at 500 °C.

The trend in the activity and stability profiles after H_2- and CO-reduction of 2 wt% Pd/CeO_2-120 at 500 °C was maintained in the presence of H_2O vapors (Fig. 3b). However, due to the concurrent water inhibition effect of Pd-based catalysts [4], the gain in activity is less pronounced for both reducing agents. Although 50 % conversion is reached around 380 °C, the highest methane conversion measured at ~500 °C for the CO-reduced catalyst is only ~95 %. Additionally, catalyst deactivation was observed already during the 1st CH_4 oxidation light-off, which is probably due to an acceleration effect of water on Pd redispersion. A drop in activity was noticed above 490 °C while heating the catalyst bed after the pre-treatment in H_2-reductive atmosphere. For the CO-reduced sample, a slight decrease in methane conversion was noticed but only above 530 °C, which is in line with the higher catalyst stability obtained by this pre-treatment.

3.3. *Structural characteristics and dynamics during catalyst pre-treatment and activity tests*

In order to better understand the structural differences leading to the same onset temperature for CH_4 oxidation but to a higher catalyst stability, the differently treated 2 wt% Pd/CeO_2-120 samples were further investigated by *ex situ and in situ* spectroscopic methods. The formation of larger particles after catalyst pre-reduction was confirmed by DRIFTS measurements conducted during CO adsorption at 30 °C (Fig. 4a, b and c). In addition to the IR bands previously attributed to CO linearly adsorbed on highly dispersed Pd species or on nanoparticle edges and corners (around 2065–2080 cm^{-1}) [45–48], CO adsorbed as bridged carbonyls on reduced Pd nanoparticles or larger clusters was observed as well around 1900–1980 cm^{-1}. The apperance of the latter, even for the as prepared catalyst, is due to the reduction of highly dispersed Pd species during CO exposure at room temperature, as it will be demonstrated in the following section. At even lower wavenumbers, features due to bridged CO adsorption on the CeO_2 surface (~1870 cm^{-1}) and at the Pd-CeO_2 interface (~1810 cm^{-1}) were identified. On low-index CeO_2 surfaces, IRRAS experiments and DFT calculations indicate that CO is adsorbed weakly with a vibrational frequency close to that of gas phase [49]. On the other hand, the frequencies close to 1850 cm^{-1} can be present due to fcc (3-fold) CO adsorbed on the Pd nanoparticle [48].

In a similar manner as reported in our previous extensive study [47], the assignments summarized in Fig. 4d were done based on DFT simulations of the vibrational frequencies of various DFT-optimized Pd structures supported on CeO_2(111), including Pd single-atoms (Pd, PdO and PdO_2), clusters (Pd_{2-3} dimers and trimers), small nanoparticles (Pd_{147} – of approx. 1.5 nm in diameter) and large nanoparticles (represented as Pd(111), Pd(100) and PdO(101) slabs). A detailed description of the generation of these models is given in the Supporting Information (pp. S25-S29), and the calculated frequencies are summarized in Table S12.

The simultaneous presence of different adsorption sites for CO is demonstrated for both catalysts. With respect to the observed difference in the noble metal particle size, the integral intensities of the bands obtained for the bridged CO in comparison to those appearing due to linearly bond CO (B/L ratios in Fig. 4) on the H_2- and CO-reduced catalysts confirm the formation of larger Pd particles in the CO pre-treated sample. This outcome is in line with the electron microscopy data (Figs. 2b and 3d) but also with previous literature on the relation between the DRIFTS data profile and the Pd particle size [48]. Additionally, different nanoparticle shapes and contact angles with the CeO_2 support can be generated during H_2- or CO-reduction of the catalysts. In our previous study [47] we assigned IR vibrational bands under 1800 cm^{-1} to CO adsorbed at the Pd-ceria interface, with CO bound to both Pd and surface oxygen from the support. An acute metal-support contact angle characteristic of spherical particles makes this stretching mode IR active while its absence could indicate the formation of hemispherical or flatter nanoparticles instead. In the experimental DRIFT spectrum the band around 1756 cm^{-1} could be attributed to the presence of such acute angles formed between more spherical Pd particles and the ceria surface in the CO-reduced catalyst. In contrast, this IR band has a lower intensity for the 2 wt% Pd/CeO_2-120 catalyst activated in 2 % H_2/Ar, which could be due to the formation of more hemispherical particles. Such a difference in the predominant noble metal particle shape suggests a different number of perimeter sites at the interface of Pd with the ceria support. Since these perimeter sites are expected to be

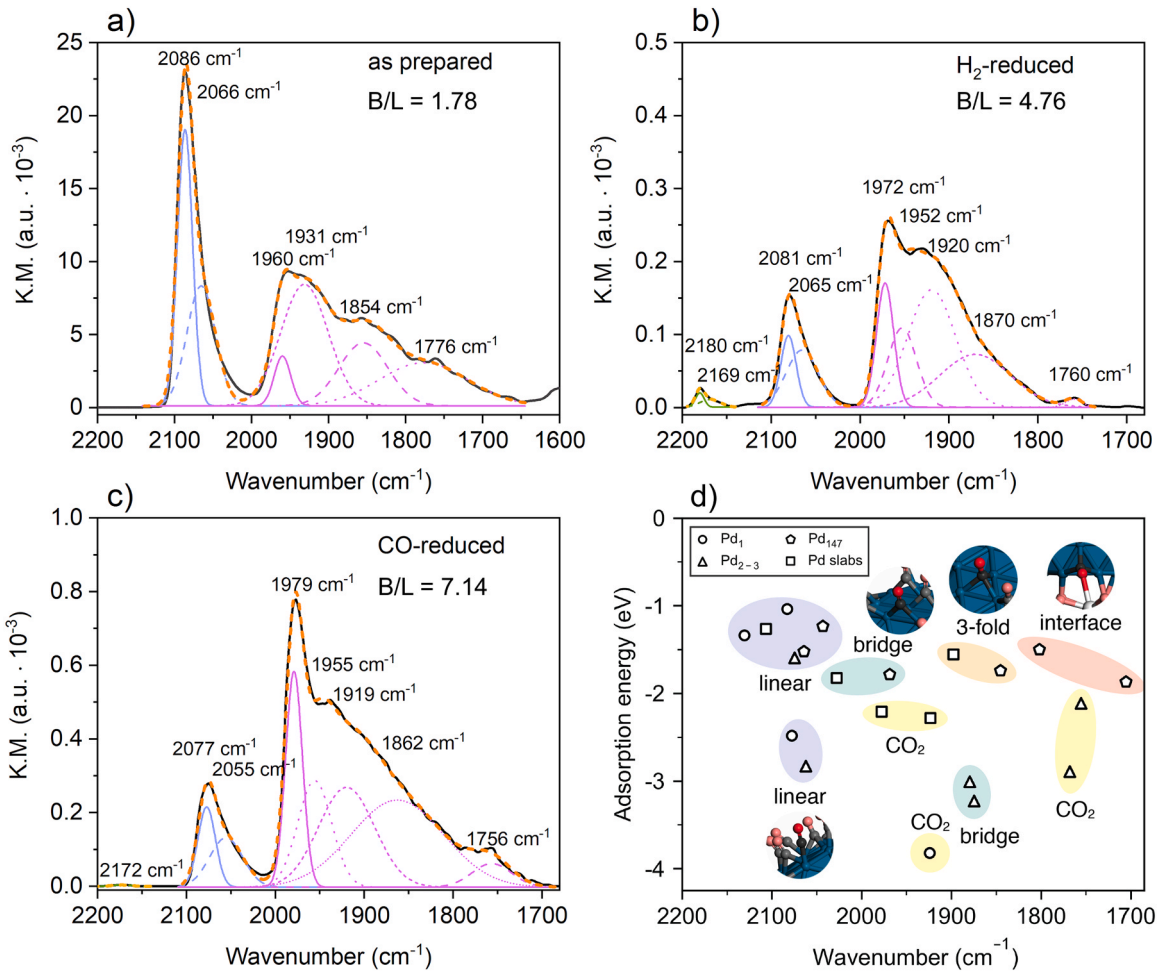

Fig. 4. DRIFTS spectra after CO adsorption at room temperature for the 2 wt% Pd/CeO_2-120 catalyst in the as prepared state (a), after H_2 reduction (b) and CO reduction (c) treatments at 500 °C for 1 h. Gas atmosphere: 1000 ppm CO/Ar. DFT-calculated wavenumbers (d) evaluated with four different types of models: Pd_1, Pd_{2-3}, Pd_{147} and Pd slabs (see pp. S25-S29 of the Supporting Information for details on the generation of these models).

the first contributors to noble metal redispersion at moderate temperatures [11], hemispherical or flatter nanoparticles are anticipated to be redispersed over the strongly interacting support faster than the more spherical Pd nanoparticles generated after activation using CO. However, besides the particle shape, multiple factors affect the experimental DRIFT spectrum, i.e. particle/cluster size, oxidation state, and CO coverage, which cannot be precisely decoupled and might contribute as well to the observed methane oxidation activity profiles.

To uncover further details on the resulting Pd states in the differently treated catalysts, X-ray absorption spectroscopy (XAS) measurements were conducted in a next step during catalyst activation and the following light-off/light-out cycles. The 2 wt% Pd/CeO_2-120 catalyst degreened at 800 °C contains predominantly highly dispersed species. The XANES spectra collected at Pd K edge show a similar profile around the white line in comparison to that obtained for a PdO reference sample (Fig. S5 a). According to the *ex situ* FT-EXAFS spectra (Fig. S5 b), Pd is completely oxidized and the interaction of most atoms with the CeO_2 support, and possibly also with hydroxyl groups from the surrounding atmosphere, is suggested by the slightly shifted scattering path appearing at 2.94 Å in comparison to the Pd-O-Pd second coordination sphere in PdO that peaks at 3.01 Å. Fig. S6 a depicts the results of the linear combination analysis (LCA) of the *in situ* XANES data collected at Pd K edge during H_2- and CO-reduction of 2 wt% Pd/CeO_2 sample. As expected, the changes in Pd^{2+} and Pd^0 concentrations between room temperature and 500 °C indicate that most Pd species are reduced in the low temperature range. In the presence of CO about 60 % of Pd is in metallic state already at 30 °C, as uncovered also by the DRIFTS measurements. Hydrogen reduces Pd^{2+} to Pd^0 at slightly higher temperature but the reaction is completed at ~160 °C. Around the same temperature only ~90 % of palladium species are reduced by CO, further reduction taking place very slowly up to 500 °C. Such a slow process might also indicate the formation of different compounds in addition to metallic Pd.

When analysing the structure of Pd after the two reduction treatments, small differences were noticed in the *ex situ* Pd K-edge XANES and FT-EXAFS profiles in comparison to the Pd metallic foil that was used as a reference (Fig. 5a and b, respectively). A slight shift of the white line towards lower energy is observed for both H_2- and CO-treated samples. This is accompanied by variations in the shape of the two main peaks of the XANES region. Additionally, the FT-EXAFS spectra indicate an increase in the Pd–Pd bond distance relative to the metallic foil (Pd foil: 2.51 Å; CO-reduced: 2.54 Å; H_2-reduced: 2.53 Å). Upon reduction and especially cooling down in the presence of hydrogen, the formation of palladium hydride is a well-known process [50,51]. Under these reaction conditions, the resulting palladium hydride phase (i.e. α or β) depends on the noble metal particle size. Particles smaller than 2 nm adsorb less and mainly surface hydrogen due to a lower number of interstitial places, whereas the formation of the more structured β-PdH_x is favoured for larger particles [52]. Similar changes in the XANES Pd K edge profile and increase in the interatomic distances were observed by Bugaev et al. [50] during selective hydrogenation of hydrocarbons. Additionally, the authors identified the formation of a stable palladium carbide phase during catalyst exposure to C_2H_2 at 100 °C, which could

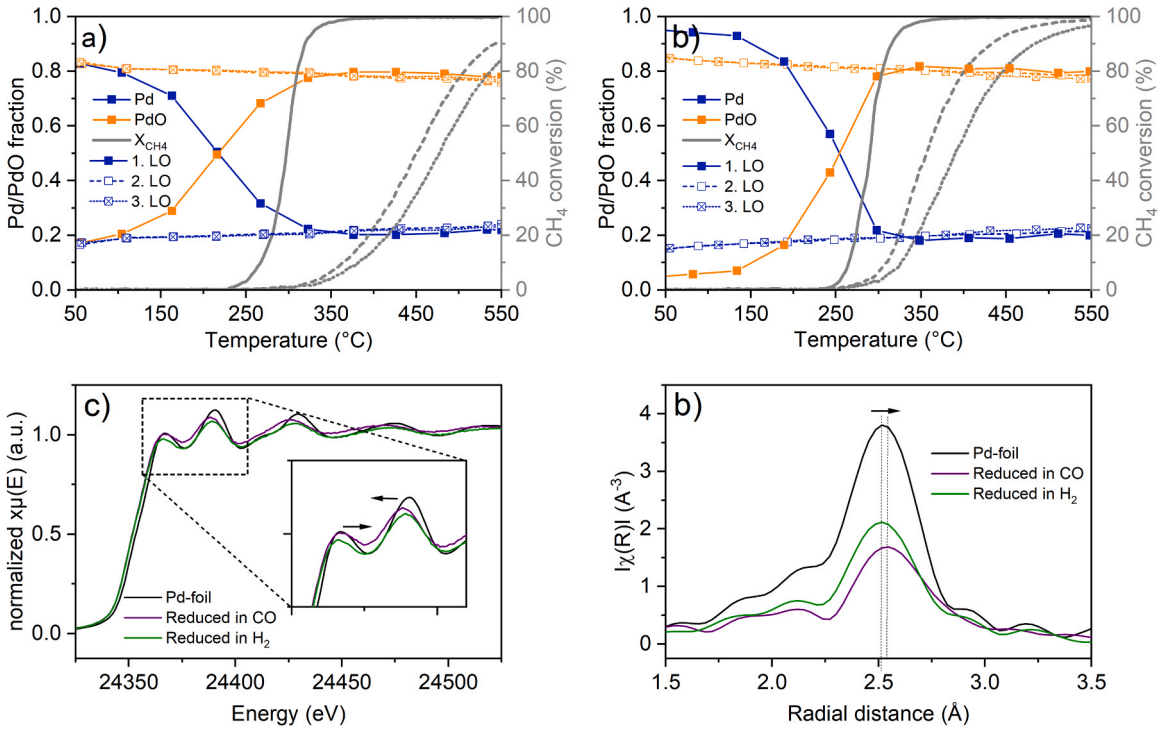

Fig. 5. XANES (a) and Fourier transformed k^3-weighted EXAFS spectra (b) collected at Pd K edge for the 2 wt% Pd/CeO_2-120 after reduction by H_2 and CO. Results of linear combination fitting of the XANES region (-20 eV to 30 eV around the edge) during 3 consecutive light-off/light-out cycles (only light-off curves are depicted) of CH_4 oxidation following catalyst activation by H_2 reduction (c) and CO reduction (d). The corresponding methane conversion measured during the *operando* XAS experiment is plotted as well.

not be reversed when applying vacuum and hydrogen at low temperatures. Carbon incorporation advances from surface/subsurface layers towards bulk [53], though the last step has a thermodynamic penalty [54,55]. The diffusion of carbon into metallic Pd lattice was reported to occur also in CO-containing atmosphere but only at higher temperatures (around 500 °C), when the breaking of C-O bond becomes possible according to Ziemecki et al. [56]. In contrast, on small noble metal particles as present in a Pd/ZrO_2 catalyst CO disproportionation via the Boudouard reaction was observed already around 100 °C, with incorporation of carbon into Pd lattice (up to 15 at%) occurring above 180 °C [57]. For this system, Maciejewski and Baiker [57] reported the complete decomposition of PdC_x around 525 °C and a high reactivity of the interstitial carbon, with its oxidation occurring already around 75 °C. According to Teschner et al. [58], the formation of the PdC_x is a surface phase and structure-sensitive reaction, leading to higher C:Pd ratios for smaller Pd particles. Based on the lattice expansion derived from the FT-EXAFS data (Fig. 4d), partial insertion of carbon into the metallic palladium lattice seems to occur also during activation of the 2 wt% Pd/CeO_2 catalyst by CO. Considering the relatively high reduction temperature applied in our study to form larger Pd nanoparticles, most probably the diffusion of carbon is favoured only at near surface defects sites [58]. Analogously, the rather small Pd nanoparticles formed at 500 °C when using H_2 as a reducing agent are expected to adsorb hydrogen during cooling mainly on the surface sites. Nonetheless, after contributing to the reduction and nanoparticle formation, both hydrogen and carbon will be removed fast in the highly oxidizing reaction conditions of methane conversion.

The Pd K edge *operando* XAS data obtained during three consecutive light-off/light-out cycles indicate that for the H_2-reduced catalyst about 60 % of Pd species are oxidized at the onset of CH_4 oxidation reaction. This result is in line with the study of Lott et al. [33] that showed that the noble metal oxidation is a prerequisite for the start of methane conversion. Further previous studies correlated a high methane oxidation activity with the presence of PdO on the particle surface or as nanoparticles/clusters [59–62] in contrast to the less active finely dispersed Pd species [63]. At 350 °C ~95 % of palladium is present as PdO in the 2 wt% Pd/CeO_2-120 sample. Overall, this state is maintained during the following activity cycles, with only a slight decrease at high temperatures. For the CO-reduced sample, about 50 % of palladium species are oxidized when methane starts to be converted. At 100 % methane conversion (360 °C) the noble metal is as well almost completely oxidized. Also in this case mainly Pd^{2+} species could be detected in the catalyst during the 2nd and 3rd L_{Off}/L_{Out} cycles. This behaviour is in agreement with a Mars van Krevelen mechanism involving lattice oxygen for C-H bond activation on the PdO surface, the generated oxygen vacancies being refiled with oxygen from the support or gas phase [3,35]. As stable intermediates, C–H breaking is known to lead to CH_3*, HCO*/HCOO* and CO* according to the DFT study of Mayernick et al. [64]. The turnover rate of methane conversion was found to be affected by the crystallite size and the density/stability of the oxygen vacancies on the surface since the Pd-O bond strength increases with the decrease of the PdO_x crystallite size [65]. Herein, undercoordinated Pd sites are required to obtain a low activation energy for the dissociative adsorption of CH_4, which is the rate-limiting step for this reaction [59,66]. However, as shown also by Chen et al. [67] via DFT calculations, Pd^{2+} ions in the square-planar PdO geometry and adjacent oxygen atoms in PdO_x NPs or clusters on ceria show excellent activity in C–H bond activation whereas Pd^{4+} in the CeO_2 lattice is poorly active for CH_4 oxidation. For CeO_2 supported catalysts, the spillover of oxygen from the support to the active Pd sites was as well identified during the fast switch to a CH_4-rich gas atmosphere [68]. Hence, various previous investigations support the trends observed in this study for the methane oxidation activity and Pd state under reaction conditions.

With respect to the overall catalyst structure, the *ex situ* Raman spectra of the differently treated samples (Fig. S9 a) are dominated by an intense band located at 464 cm^{-1}, which has been previously assigned to the F_{2g} vibrational mode of the CeO_2 fluorite phase [69]. Only a minor shift of this band is noticed between the fresh and treated catalysts. The

weak and broad band between 520 and 590 cm^{-1} corresponds to defect-induced (D) mode (oxygen vacancies) [70]. The band at 645 cm^{-1} arises due to the presence of crystalline PdO traces (B_{1g} mode) [71–73]. The band at 828 cm^{-1} corresponds to stretching vibration of peroxo species that could be located at the interface between Pd and CeO_2 support [72]. Both bands appear to be more pronounced after CO reduction and especially at the end of the CH_4 oxidation cycles, in line with the formation of larger PdO nanoparticles.

The analysis of the XAS data obtained at the end of the 3rd L_{Off}/L_{Out} cycle shows that Pd is again in highly dispersed state, almost irrespective of the applied pre-reduction treatment. The FT-EXAFS spectra depicted in Fig. S7 reveal a very similar profile of the first and second coordination spheres as observed for the degreened 2 wt% Pd/CeO_2 catalyst. The redispersion of noble metal particles already at these relatively mild temperatures has been previously demonstrated for Pt/CeO_2 catalysts [11], and it is shown here to occur also for Pd. Overall, the strong interaction between Pd and CeO_2 prevents the noble metal from sintering and permanent loss of active sites. However, within the typical working temperature range of the methane oxidation catalyst, this interplay leads as well to pronounced redispersion of the noble metal, which is accompanied by a severe decrease in activity. As demonstrated in the following, the course of this process is influenced by two interrelated factors: the noble metal concentration and support surface area.

3.4. *Effect of noble metal concentration on CeO_2 surface*

To evaluate the effect of the noble metal concentration, Pd loading was varied between 1 and 3 wt% on the CeO_2-120 support with high surface area. Table S1 reports the corresponding elemental composition, BET surface area and pore volume for the three catalysts. This change in catalyst composition results in a noble metal coverage on the support of about 20 %, 40 % and 60 % of a monolayer, respectively, assuming that only Pd single sites are formed at four-folded hollow locations on the ceria support [13]. Detailed information on the calculation procedure is provided in SI (Table S3). In agreement with the theoretical monolayer coverage, the XRD patterns collected for the three samples show no characteristic reflections for PdO or metallic Pd, suggesting a high dispersion of the noble metal in all cases (Fig. S8). The *ex situ* Raman spectra of the differently loaded CeO_2-120 catalysts (Fig. S9 b) show a small red shift for the F_{2g} band and an increase of the D band intensity around 590 cm^{-1}, which could indicate a higher number of defects in the CeO_2 structure due to the interaction with the noble metal species. At the same time, the band corresponding to Pd-O vibration at 648 cm^{-1} is also increasing for higher Pd loadings, which is in agreement with the formation of crystalline PdO.

For the activity tests, the catalyst amount was adjusted to maintain the same noble metal WHSV. Hence, the observed differences in activity are mainly affected by the noble metal state. After the high temperature treatment in oxidizing atmosphere, a higher activity was obtained only for the 3 wt% Pd/CeO_2-120 sample in comparison with the other two catalysts containing 1 and 2 wt% Pd (Fig. 6a). About 35 % CH_4 conversion at 550 °C and a reaction onset at 400 °C were measured for the highly loaded catalyst whereas only ~10 % methane oxidation was reached for the 1 and 2 wt% Pd/CeO_2-120 samples at a total gas flow of 1 L/min. According to the HAADF-STEM EDXS maps reported in Fig. S10, at low loadings Pd is highly dispersed and homogeneously distributed on ceria. In contrast, the formation of noble metal agglomerates is observed for the catalysts containing 3 wt% Pd loading. This indicates that the Pd-O-Ce bond formation is restricted to specific surface sites, e.g. surface lattice defects, since the noble metal loading is below the theoretical monolayer coverage for this sample (60 %). Although we cannot exclude an effect of the electron beam, this outcome is in line with the previous study of Maurer et al. [12] on Pt/CeO_2 showing that cluster formation occurs above a certain noble metal

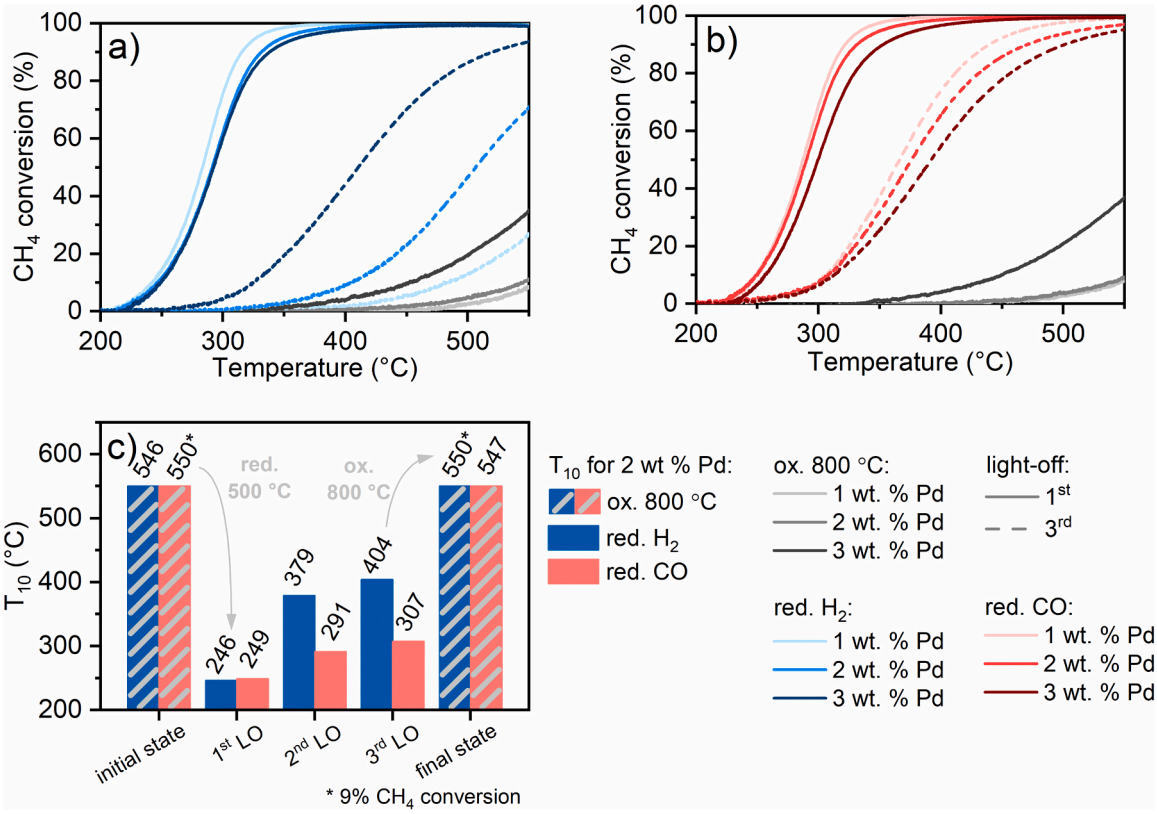

Fig. 6. Influence of Pd loading on the rate of methane conversion of the H_2- (a) and CO- (b) reduced Pd/CeO_2-120 catalysts over three light-off/light-out cycles (only light-off curves are depicted). (c) Comparison of the temperatures for 10 % methane conversion in dry atmosphere for the 2 wt%Pt/CeO_2-120 catalyst activated by CO- and H_2-reduction.

concentration on ceria surface. Herein, this process is confirmed even after the high temperature treatment in oxidizing atmosphere, which seems to have a direct impact on the activity profile.

As demonstrated in the following, this limit of the noble metal dispersion on the strongly interacting CeO_2 influences also the formation of nanoparticles during catalyst pre-treatment procedure and the redispersion process under reaction conditions. As illustrated in Figs. 6a and 6c, after catalyst reduction in H_2-containing atmosphere a significant improvement in activity is obtained for all samples. The smaller Pd particles formed at low noble metal loadings (Fig. 6a and S11 a) have a higher number of active sites, thus, the lowest T_{50} temperature was measured for the 1 wt% Pd/CeO_2-120 sample after catalyst reduction. However, this sample shows also the lowest stability during the three consecutive light-off/light-out methane oxidation cycles. The 3 wt% Pd/CeO_2-120 catalyst is able to convert 50 % of methane around 410 °C during the third activity light-off, whereas the 1 wt% Pd/CeO_2-120 catalyst shows less than 30 % conversion even at 550 °C, despite the same total amount of noble metal being present in the plug-flow reactor during both catalytic tests.

To better understand the Pd redispersion process, ETEM investigations were conducted for the 3 wt% Pd/CeO_2-120 catalyst during exposure to reducing and oxidizing conditions. Due to the low contrast, the structural changes of the catalyst could not be monitored by TEM. Instead, EDX mapping of the same area was obtained at room temperature after exposure of the catalyst to reductive or oxidizing gases at different temperatures. Initially, the sample was *in situ* pre-reduced in 18 mbar H_2 at 500 °C in the ETEM, which resulted in the formation of metallic Pd particles of 1–10 nm (Fig. 7a and S11a), unevenly distributed at the nm scale. The *in situ* reduction of noble metal species is confirmed by the crystal structure and lattice parameters derived from the fast Fourier transform (FFT) patterns (Fig. S13). In 10 mbar O_2 the noble metal redispersion/redistribution is already detected at 300 °C (Fig. S12). This is indicated in Fig. S12 by the disappearance of the small noble metal clusters and the apparent increase in size of larger nanoparticles. The latter phenomenon can be explained by the formation of the PdO phase and migration of atoms at perimeter sites with the ceria support, resulting in noble metal particle flattening. This process is accelerated at higher temperatures (Fig. S12 c). As a result, a more homogeneous distribution of Pd on CeO_2 is obtained, evidenced by the increased brightness of the images.

The early redispersion and the impact of the temperature on the redispersion rate was identified also during the catalytic tests. By limiting the temperature range for the light-off/light-out tests to $\leq$ 500°C, the drop in the methane oxidation activity is less pronounced in comparison to the measurements up to 550°C (Fig. S22 versus Fig. 6a). Although the formation of smaller and active Pd clusters cannot be excluded, it can be generally assumed based on the ETEM results that the redispersion process occurs mainly at the interface with CeO_2. This leads to the formation of strongly interacting Pd species, i.e. single sites, which are not expected to contribute to the CH_4 conversion.

By careful analysis of the EDX maps collected after exposing the 3 wt % Pd/CeO_2-120 for 10 minutes to 10 mbar O_2 at 800 °C (Fig. 7b), several general trends could be identified: (i) small nanoparticles (< 5 nm) at locations with low noble metal surface concentration are

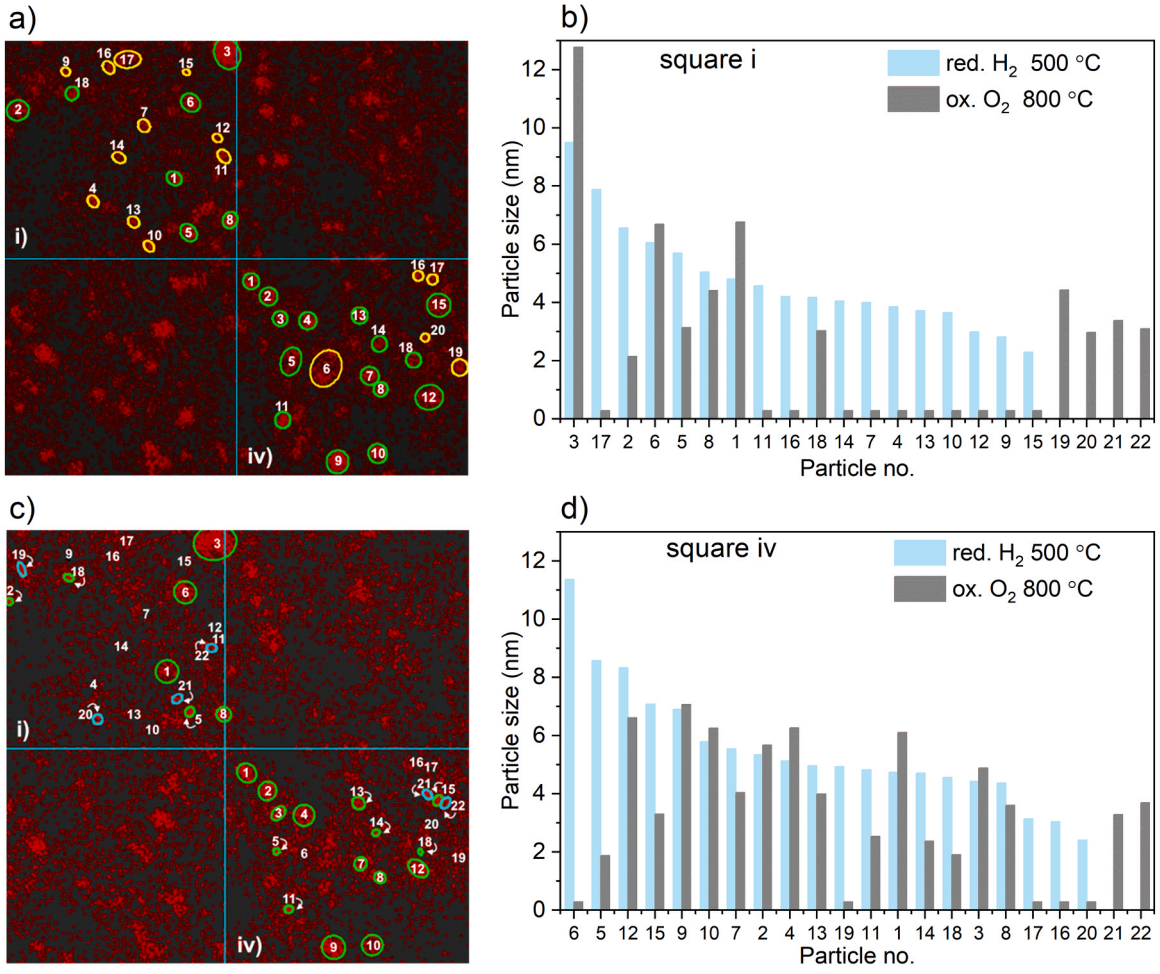

Fig. 7. EDXS-maps of the 3.0 wt% Pd/CeO_2-120 catalyst after pre-reduction in 18 mbar H_2 at 500 °C (a) and oxidation for 10 minutes in 10 mbar O_2 at 800 °C (c). The corresponding sizes for the particles marked in sections i) and iv) are shown in (b) and (d) for the two different treatments: red. H_2 500 °C and ox. O_2 800 °C.

completely redispersed (marked by blue circles in Fig. S12) whereas the redispersion is only partial for larger particles; (ii) during short exposure to high temperature as applied during the *in situ* ETEM experiments, the redispersion of both small and large particles is constrained at locations where Pd concentration on the support surface is high (marked by yellow circles in Fig. S12). This final observation suggests a surface saturation threshold, reached once Pd atoms occupy all available sites and the migration over longer distances is not favoured by the reaction conditions.

Catalyst activation in CO-containing atmosphere leads to similar trends in the activity improvement and stability for the differently loaded Pd/CeO_2-120 catalysts (Fig. 6b). In all cases, a smaller decrease in activity was observed in comparison to that shown by the corresponding H_2-reduced samples (Table S2). Additionally, all CO-reduced samples maintained a reasonable methane conversion profile during the 3rd L_{Off}, with the 1 wt% Pd/CeO_2-120 showing the best low-temperature activity (T_{50} at 366 °C vs. 376 °C measured for the 2 wt% and 392 °C for 3 wt% Pd catalyst). In the presence of water vapours, the CO-activated catalysts showed the same light-off temperature of 361 °C during the first light-off, irrespective of the noble metal loading (Table S2). Overall, despite the more pronounced deactivation recognized in comparison to the dry reaction conditions, the CH_4 oxidation activity did not vary significantly among the 1 wt%, 2 wt% and 3 wt% Pd catalysts. The 3 wt% Pd/CeO_2 catalyst exhibited only a slightly lower drop in activity during the 3rd light-off (T_{50} at 432 °C), followed by the 2 wt% Pd (T_{50} at 456 °C) and 1 wt% Pd (T_{50} at 456 °C) samples. These very similar behaviours point to a similar Pd state in the differently loaded catalysts.

According to the EDXS maps obtained for the CO reduced 1 wt% and 3 wt% Pd/CeO_2-120 samples (Fig. S11 b), both contain a high number of large nanoparticles with sizes of up to 7 nm. This is in contrast to the corresponding H_2-reduced catalysts, where a clear difference in noble metal particle size was observed, namely larger nanoparticles are formed for higher Pd loadings. In agreement, similar CO-adsorption DRIFTS spectra were collected for the 1 wt% and 3 wt% Pd/CeO_2-120 catalysts after CO-reduction (Fig. S14). In both cases, bands corresponding to CO adsorbed as bridged carbonyls on reduced Pd nanoparticles or larger clusters appear at 1900–1980 cm^{-1}. These results suggest that the relatively long catalyst pre-treatment of 1 h combined with the CO-assisted noble metal sintering [42,43] leads to a very similar noble metal state in all samples. Consequently, the oxidation of Pd particles and their redispersion under lean reaction conditions are, in a first stage, not affected significantly by the noble metal loading, but mostly by the release and diffusion of Pd atoms on the support surface. Hence, the similar deactivation rates observed for the 1 wt%, 2 wt% and 3 wt% Pd/CeO_2-120 catalysts over the three light-off/light-out cycles up to 550 °C can be associated with a comparable noble metal redispersion rate. However, during a hypothetical next stage of the redispersion process that corresponds to diminished sizes for Pd nanoparticles, the noble metal concentration on the surface of ceria is expected to affect the evolution of the catalyst, as demonstrated for the H_2-reduced Pd/CeO_2 catalysts (Fig. 6a). In the long term, for noble metal loadings exceeding the achievable monolayer coverage complete redispersion does not occur. As illustrated in the following section, the inefficient use of the noble metal can be prevented by tuning the monolayer concentration via decreasing the support surface area.

3.5. *Effect of CeO_2 surface area*

To further substantiate these findings and identify the theoretical threshold for the formation of active Pd clusters or nanoparticles, a series of catalysts containing between 2 and 3 wt% Pd supported on CeO_2 with different surface areas (30, 60 and 120 m^2/g) was additionally prepared. For the 2 wt% Pd/CeO_2-60 catalyst 80 % of the single site monolayer coverage is achieved whereas the monolayer is exceeded for the 3 wt% Pd/CeO_2-60 (120 %) and 2 wt% Pd/CeO_2-30 (176 %) samples (Table S3). For all catalytic tests a gas mixture containing 3200 ppm CH_4, 10 %O_2 in N_2 was used at a total flow of 1 L/min. Fig. 8 illustrates the trends in activity obtained after calcination at 800 °C for 10 h and CO reduction at 500 °C for 1 h. In comparison to the 2 wt% Pd/CeO_2-120 catalyst (Fig. 1a), both catalysts containing the same noble metal loading but supported on ceria with lower surface areas show a methane oxidation reaction onset below 300 °C after degreening for 10 h in air at 800 °C. In line with the assumptions derived in the above sections, the exhibited activity must be linked to the presence of larger palladium clusters or nanoparticles that are formed due to the higher noble metal concentration in these samples on the ceria surface unit. However, the complete conversion of methane is not reached in both cases, despite the double noble metal monolayer concentration in the 2 wt% Pd/CeO_2-30 sample. At 550 °C a maximum of 72 % conversion was measured for the 2 wt% Pd/CeO_2-30 catalyst whereas the 2 wt% Pd/CeO_2-60 sample converted 65 % of methane. Considering the different properties of these two samples, the rather similar activity profiles cannot represent the fingerprint of an identical noble metal state. While the entire Pd amount is potentially redispersed at 800 °C in the 2 wt% Pd/CeO_2-60 sample, the exceeding amount of noble metal relative to the single site monolayer as present in the 2 wt% Pd/CeO_2-30 catalyst is expected to sinter or agglomerate under these extreme temperature conditions. This hypothesis is reinforced by the EDX maps obtained for the 3 wt% Pd/CeO_2-60 catalyst after calcination for 10 h at 800 °C, which uncover very large PdO agglomerates/particles of over 10 nm alongside highly dispersed Pd species (Fig. S15). As a result of the higher noble metal concentration on ceria surface unit, even larger noble metal nanoparticles are expected to form on the CeO_2-30 support due to sintering. Hence, even though CeO_2 is a strongly interacting support and a concentration of 2–3 wt% Pd is a largely applied noble metal loading, such high temperature treatments might lead to significant and permanent noble metal loss since only part of Pd will redisperse on low surface area supports.

The inefficient use of the noble metal on the CeO_2-30 support is visible also in the activity profiles obtained after CO activation. The 2 wt % Pd/CeO_2-60 catalyst shows lower T_{50} temperatures for all three light-offs in comparison to the values measured for the 2 wt%Pd/CeO_2-30 sample, which is most probably caused by the smaller noble metal particles and higher number of surface sites formed on the ceria support with a higher surface area.

By further increasing the noble metal loading on the CeO_2-60 support to 3 wt% Pd, the theoretical noble metal monolayer coverage is only slightly exceeded (120 %). For this sample 50 % CH_4 conversion is obtained at 454 °C after the thermal treatment at 800 °C, and 90 % of methane is oxidized at 550 °C. After activation by CO reduction, this catalyst shows also the highest low-temperature activity during the following light-offs. However, at this noble metal loading very large particles are formed already during the catalyst calcination step at 800 °C (Fig. S15). In this case, the formation of homogeneously distributed particles with a narrow size distribution during catalyst application requires careful screening of the pre-treatment/activation procedures. Alternatively, the noble metal loading can be further adjusted to prevent the formation of such large noble metal particles.

To gain a better understanding of the relationship between the noble metal loading, the support surface area and the catalyst activity/stability behaviour, reaction rates of methane oxidation were calculated per unit mass of noble metal at 300 °C for all catalysts investigated in this study, including the measurements conducted after the different pre-treatment procedures (Fig. 9, Table S4). Since not all samples exhibited detectable conversions at this temperature, a linear regression based on the Arrhenius equation was used to calculate the reaction rate at 300 °C (see p. S13 of the SI, Fig. S16, tables S5-S12 for the details) for each catalyst. The corresponding calculations are shown in Fig. S16 and Table S4. This approach was used since an accurate estimation of the number of surface atoms cannot be done for such dynamic systems (i.e. calculation of turnover numbers), as the Pd particle size varies during

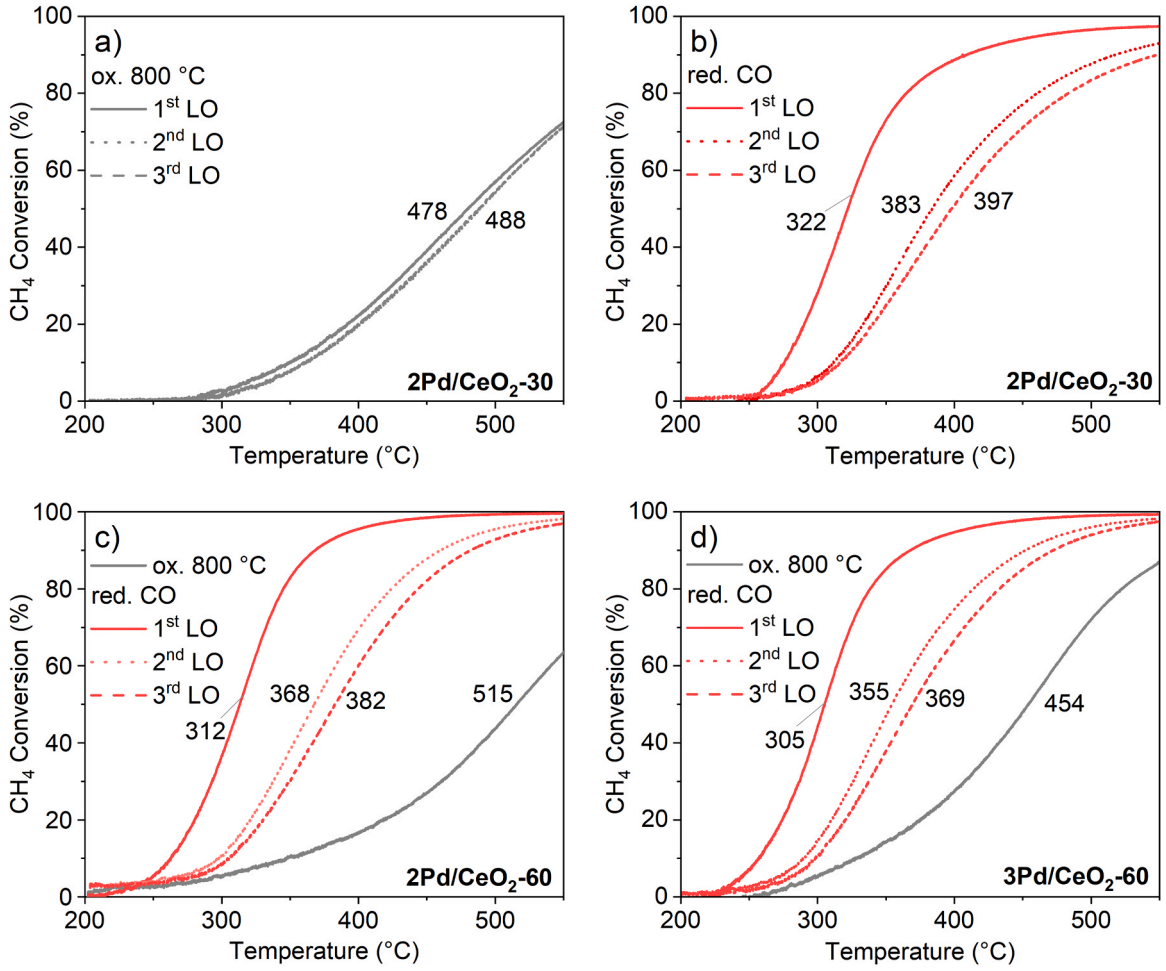

Fig. 8. CH_4 oxidation activity over 3 consecutive light-offs for 2 wt% Pd/CeO_2-30 after thermal treatment at 800 °C in air (a) and reduction in 0.5 % CO/N_2 for 1 h at 500 °C (b). CH_4 conversion for the 2 wt% Pd/CeO_2-60 (c) and 3 wt%Pd/CeO_2-60 (d) after oxidative treatment at 800 °C and activation by CO-reduction at 500 °C for 1 h. Gas mixture: (a) 3200 ppm CH_4, 10 vol% O_2 in N_2; (b) 3200 ppm CH_4, 5 vol% H_2O, 10 vol% O_2 in N_2 at a weight hourly space velocity of 20000 $L{\cdot}g_{NM}^{-1}{\cdot}h^{-1}$. The temperature of 50 % CH_4 conversion is indicated next to each conversion curve.

methane oxidation light-off. However, by describing the reaction rates in relation to the corresponding Pd single site monolayer coverage (Fig. 9) all possible Pd states that can be generated under reaction conditions are hypothetically considered.

The following observations can be derived from the comparison of the reaction rates as a function of the monolayer coverage:

a. After degreening at 800 °C in air and reaching the maximum redispersion degree, the catalysts exhibit significant differences in their activities depending on their particular surface noble metal concentrations. The rate of methane oxidation grows exponentially as the theoretically possible monolayer of Pd single atoms on CeO_2 surface fills (almost three orders of magnitude reaction rate increase upon the monolayer coverage changes from ~ 20 to 80 %. Around the complete monolayer coverage (80–120 %), the reaction rate stabilizes at its highest values, plausibly due to the formation of particles with optimal dispersion. Further increase of the noble metal coverage leads to the activity diminishment, most likely caused by the formation of large Pd nanoparticles and loss of surface sites.
b. Reductive treatments boost methane oxidation activity of Pd/CeO_2 catalysts by one to several orders of magnitude. As confirmed by the electron microscopy, *in situ/operando* XAS, Raman spectroscopy and DRIFTS investigations, this is due to the increase of Pd particle size that occurs especially in the presence of CO. Under reaction conditions, Pd nanoparticles/clusters are reoxidized prior to the reaction onset, and the resulting Pd^{2+} species in PdO like structures contribute to C-H activation. The highest methane oxidation rates were obtained for the 800 °C-degreened Pd/CeO_2-120 catalysts with high surface area, immediately after pre-reduction in CO or H_2. Only small variations were observed by changing the noble metal loading between 1 and 3 wt% due to the relatively long pre-treatment time and CO-assisted sintering of Pd species. The observed rates are up to four times higher in comparison with those measured for the CeO_2-60 and CeO_2-30 catalysts. However, Pd/CeO_2-120 catalysts are prone to fast deactivation.
c. The highest stability is shown by the Pd/CeO_2 catalysts with a noble metal loading of about 0.3–0.5 mg/m^2 that corresponds to about 80–120 % filling of the theoretical single site monolayer coverage. This is evidenced by the considerably high reaction rates in the second and especially third light-offs after reduction. For this range of noble metal concentrations most of Pd loading is not only efficiently used but also enables the recovery of the highly dispersed noble metal state after oxidative treatment (see also Fig S17). The redispersion and reduction approach is not applicable for the sample with the highest noble metal surface coverage, i.e. 2 wt% Pd/CeO_2-30. Although it demonstrates a considerable activity and stability after the least demanding treatment (oxidation at 500 °C), both its oxidation at 800 °C and its reduction provide states that are less active than those of more optimal catalysts under analogous

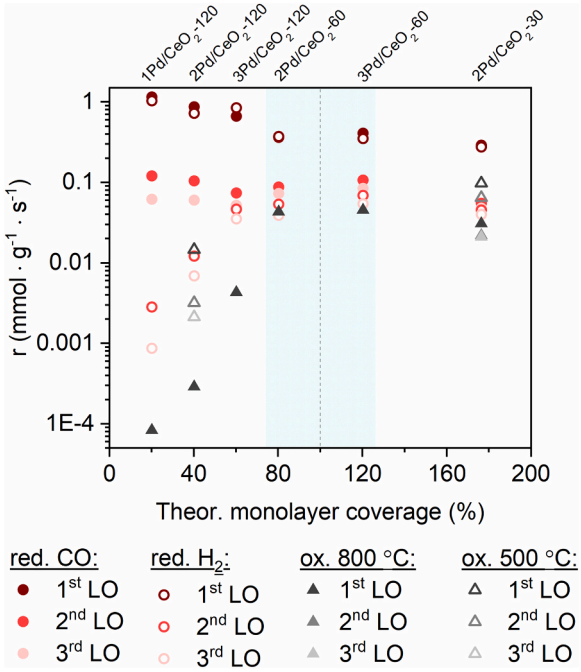

Fig. 9. Integral reaction rates of CH_4 oxidation at 300 °C for the different samples investigated in this study as a function of the theoretical monolayer coverage of Pd single sites on CeO_2 surface (see p. S12 in the SI). As reported in the previous sections 4.1–4.4, all samples were tested during consecutive light-offs in the as prepared state (ox. 500 °C), after oxidative (ox. 800 °C) and reductive treatments (red. H_2; red. CO at 500 °C for 1 h). The optimal Pd loading on pure ceria for achieving high activity and efficient noble metal usage is marked with light blue.

conditions. Under the studied conditions, optimal catalyst parameters were obtained for the CeO_2-60 support at 2–3 wt% Pd loading.

d. Two deactivation processes can be identified for Pd/CeO_2 methane oxidation catalysts, their extent depending on the noble metal loading and ceria properties. On the one hand, noble metal redispersion occurs at high temperatures leading to formation of highly dispersed and inactive species. On the other hand, at high noble metal loadings per ceria surface area unit that exceed the theoretical monolayer coverage, sintering and agglomeration take place at high temperatures, irrespective of the gas atmosphere. This latter process leads to a quasi-permanent loss of the noble metal, similar to that observed on non-interacting catalyst carriers.

4. Conclusions

This study reports a systematic investigation of the catalytic behavior and structural peculiarities of Pd/CeO_2 catalysts for complete methane oxidation. By varying the noble metal loading and ceria properties as well as the catalyst pre-treatment procedure we were able to elucidate essential aspects that need to be considered already during catalyst preparation for achieving a high low-temperature activity combined with good catalyst durability under reaction conditions. Complementary characterization by electron microscopy, Raman spectroscopy, DRIFTS and *in situ/operando* XAS supplemented by DFT calculations allowed to correlate the formation of small Pd nanoparticles with a high CH_4 conversion whereas highly dispersed Pd single sites or very small clusters proved to be poorly active for this reaction. The optimal noble metal particle size can be achieved by reductive treatments of highly dispersed catalysts. The performance depends on the reduction agent, time and temperature of reduction. In line with previous studies, the oxidation of the formed Pd nanoparticles occurs under reaction conditions prior to the methane oxidation onset, and the resulting Pd^{2+} species in PdO contribute to C-H activation. Notably, for high temperature reactions such as methane oxidation, pronounced noble metal redispersion is concurrently encountered in lean atmosphere if a high surface area CeO_2 (>100 m^2/g) is used. According to the ETEM investigations, this process starts above 300 °C and leads to rapid catalyst deactivation as the reaction temperature increases. Although slightly larger and more stable Pd nanoparticles were obtained by CO-reduction in comparison to a H_2-reductive treatment, pronounced loss in catalyst activity was observed over several light-off/light-out cycles on the high surface area ceria supports. On the contrary, for similar noble metal loadings the exposure to high temperatures results simultaneously in strong noble metal sintering if a low surface area CeO_2 (~30 m^2/g) is employed during catalyst preparation. This later process takes place irrespective of the gas atmosphere, and leads to a quasi-permanent loss of a fraction of noble metal sites.

To prevent catalyst deactivation while still exploiting the interaction with CeO_2, a threshold in the noble metal loading was identified in this study. This corresponds to a noble metal concentration around the theoretical single site monolayer coverage. Our results suggest that a Pd loading of about 0.3–0.5 mg/m^2, which corresponds to a theoretical single site monolayer coverage between 80 % and 120 %, is sufficient to achieve a high low-temperature activity and especially long-term stability over the entire temperature range of CH_4 oxidation. This includes high gas-hourly space velocity conditions as applied in this work. Finally, by adjusting the noble metal loading and the ceria properties, an efficient use of the noble metal is ensured since both deactivation processes, i.e. redispersion and sintering, are rationally controlled.

CRediT authorship contribution statement

Mimoun Aouine: Writing – review & editing, Investigation, Formal analysis, Data curation. **David Loffreda:** Writing – review & editing, Software, Methodology, Funding acquisition, Formal analysis, Data curation, Conceptualization. **Philippe Vernoux:** Writing – review & editing, Validation, Resources, Project administration, Methodology, Funding acquisition, Formal analysis. **Stéphane Loridant:** Writing – review & editing, Funding acquisition, Formal analysis. **Deniz Zengel:** Writing – original draft, Methodology, Investigation, Formal analysis, Data curation, Conceptualization. **Maria Casapu:** Writing – original draft, Validation, Supervision, Methodology, Funding acquisition, Formal analysis, Data curation, Conceptualization. **Heike Störmer:** Writing – review & editing, Formal analysis, Data curation. **Merve Kurt:** Writing – review & editing, Investigation, Formal analysis, Data curation. **Jan-Dierk Grunwaldt:** Writing – review & editing, Validation, Supervision, Resources, Project administration, Methodology, Funding acquisition, Formal analysis, Conceptualization. **Vasyl Marchuk:** Writing – original draft, Investigation, Formal analysis, Data curation. **Agustin Salcedo:** Writing – original draft, Investigation, Formal analysis, Data curation. **Florian Maurer:** Writing – review & editing, Investigation, Formal analysis, Data curation. **Carine Michel:** Writing – review & editing, Supervision, Software, Resources, Project administration, Methodology, Funding acquisition, Formal analysis, Conceptualization.

Declaration of Competing Interest

The authors declare that they have no known competing financial interests or personal relationships that could have appeared to influence the work reported in this paper.

Data Availability

Data will be made available on request.

Acknowledgements

The authors acknowledge the financial support from the Agence Nationale de la Recherche (grant No. ANR-19-CE05-0038, PRCI DYCAT project) and the Deutsche Forschungsgemeinschaft (DFG, German Research Foundation; grant No. 431423888 DYCAT project). JDG, DZ, VM and MK gratefully thank DFG (GR 3987/18-1) and KIT for financial support. VM and FM thank DFG (German Research Foundation) for the financial support via the SFB 1441 – Project-ID 426888090. We acknowledge SOLEIL for provision of synchrotron radiation facilities and we would like to thank Dr. Emiliano Fonda, Dr. Gautier Landrot and Dr. Andrea Zitolo for their great support and assistance in using the SAMBA beamline (Proposal No. 20220609). We acknowledge the PSMN mesocenter in Lyon for CPU time and assistance (CPER/SYSPROD 2015–2022 project No.~2019-AURA-P5B and AXELERA Pôle de compétitivité). We thank Dr. Thomas Bergfeldt (IAM-AWP, KIT) for the ICP-OES elemental analysis measurements, Markus Makowiak (ITCP, KIT) for the N_2-physisorption experiments and Kevin Keller (ITCP, KIT) for providing one sample for this study.

Appendix A. Supporting information

Supplementary data associated with this article can be found in the online version at doi:10.1016/j.apcatb.2024.124363.

References

[1] A.E. Hughes, N. Haque, S.A. Northey, S. Giddey, Platinum group metals: a review of resources, production and usage with a focus on catalysts, Resources 10 (2021) 93.
[2] P. Lott, M. Casapu, J.-D. Grunwaldt, O. Deutschmann, A review on exhaust gas after-treatment of lean-burn natural gas engines – from fundamentals to application, Appl. Catal. B 340 (2024) 123241.
[3] D. Ciuparu, M.R. Lyubovsky, E. Altman, L.D. Pfefferle, A. Datye, Catalytic combustion of methane over palladium-based catalysts, Catal. Rev. 44 (2002) 593–649.
[4] D. Ciuparu, L. Pfefferle, Support and water effects on palladium based methane combustion catalysts, Appl. Catal. A 209 (2001) 415–428.
[5] B.A. Raj, Methane Emission Control, Johns. Matthey Technol. Rev. 60 (2016) 228–235.
[6] A. Gremminger, P. Lott, M. Merts, M. Casapu, J.-D. Grunwaldt, O. Deutschmann, Sulfur poisoning and regeneration of bimetallic Pd-Pt methane oxidation catalysts, Appl. Catal. B 218 (2017) 833–843.
[7] N. Sadokhina, G. Smedler, U. Nylen, M. Olofsson, L. Olsson, Deceleration of SO_2 poisoning on PtPd/Al_2O_3 catalyst during complete methane oxidation, Appl. Catal. B 236 (2018) 384–395.
[8] T. Franken, M. Roger, A.W. Petrov, A.H. Clark, M. Agote-Aran, F. Krumeich, O. Kröcher, D. Ferri, Effect of short reducing pulses on the dynamic structure, activity, and stability of Pd/Al_2O_3 for wet lean methane oxidation, ACS Catal. 11 (2021) 4870–4879.
[9] A.W. Petrov, D. Ferri, O. Krocher, J.A. van Bokhoven, Design of stable palladium-based zeolite catalysts for complete methane oxidation by postsynthesis zeolite modification, ACS Catal. 9 (2019) 2303–2312.
[10] M.S. Wilburn, W.S. Epling, Sulfur deactivation and regeneration of mono-and bimetallic Pd-Pt methane oxidation catalysts, Appl. Catal. B 206 (2017) 589–598.
[11] A.M. Gänzler, M. Casapu, P. Vernoux, S. Loridant, F.J. Cadete Santos Aires, T. Epicier, B. Betz, R. Hoyer, J.D. Grunwaldt, Tuning the structure of platinum particles on ceria in situ for enhancing the catalytic performance of exhaust gas catalysts, Angew. Chem. Int. Ed. 56 (2017) 13078–13082.
[12] F. Maurer, A. Beck, J. Jelic, W. Wang, S. Mangold, M. Stehle, D. Wang, P. Dolcet, A. M. Gänzler, C. Kübel, Surface noble metal concentration on ceria as a key descriptor for efficient catalytic CO oxidation, ACS Catal. 12 (2022) 2473–2486.
[13] F. Maurer, J. Jelic, J. Wang, A. Gänzler, P. Dolcet, C. Wöll, Y. Wang, F. Studt, M. Casapu, J.-D. Grunwaldt, Tracking the formation, fate and consequence for catalytic activity of Pt single sites on CeO_2, Nat. Catal. 3 (2020) 824–833.
[14] A.M. Gänzler, M. Casapu, F. Maurer, H. Störmer, D. Gerthsen, G. Ferre, P. Vernoux, B. Bornmann, R. Frahm, V. Murzin, Tuning the Pt/CeO_2 interface by in situ variation of the Pt particle size, ACS Catal. 8 (2018) 4800–4811.
[15] K. Keller, P. Lott, S. Tischer, M. Casapu, J.D. Grunwaldt, O. Deutschmann, Methane oxidation over PdO: Towards a better understanding of the influence of the support material, ChemCatChem 15 (2023) e202300366.
[16] S. Brunauer, P.H. Emmett, E. Teller, Adsorption of gases in multimolecular layers, JACS 60 (1938) 309–319.
[17] B. Ravel, M. Newville, ATHENA, ARTEMIS, HEPHAESTUS: data analysis for X-ray absorption spectroscopy using IFEFFIT, J. Sychrotron Rad. 12 (2005) 537–541.
[18] G. Kresse, J. Furthmüller, Efficient iterative schemes for ab initio total-energy calculations using a plane-wave basis set, Phys. Rev. B 54 (1996) 11169.
[19] G. Kresse, J. Hafner, Ab initio molecular dynamics for liquid metals, Phys. Rev. B 47 (1993) 558.
[20] J.P. Perdew, M. Ernzerhof, K. Burke, Rationale for mixing exact exchange with density functional approximations, J. Chem. Phys. 105 (1996) 9982–9985.
[21] S. Grimme, J. Antony, S. Ehrlich, H. Krieg, A consistent and accurate ab initio parametrization of density functional dispersion correction (DFT-D) for the 94 elements H-Pu, J. Chem. Phys. 132 (2010).
[22] S. Grimme, S. Ehrlich, L. Goerigk, Effect of the damping function in dispersion corrected density functional theory, J. Comput. Chem. 32 (2011) 1456–1465.
[23] P.E. Blöchl, Projector augmented-wave method, Phys. Rev. B 50 (1994) 17953.
[24] G. Kresse, D. Joubert, From ultrasoft pseudopotentials to the projector augmented-wave method, Phys. Rev. B 59 (1999) 1758.
[25] S.L. Dudarev, G.A. Botton, S.Y. Savrasov, C. Humphreys, A.P. Sutton, Electron-energy-loss spectra and the structural stability of nickel oxide: An LSDA+ U study, Phys. Rev. B 57 (1998) 1505.
[26] M.V. Ganduglia-Pirovano, J.L. Da Silva, J. Sauer, Density-functional calculations of the structure of near-surface oxygen vacancies and electron localization on CeO_2 (111), Phys. Rev. Lett. 102 (2009) 026101.
[27] M.V. Ganduglia-Pirovano, A. Hofmann, J. Sauer, Oxygen vacancies in transition metal and rare earth oxides: Current state of understanding and remaining challenges, Surf. Sci. Rep. 62 (2007) 219–270.
[28] C. Loschen, J. Carrasco, K.M. Neyman, F. Illas, First-principles LDA+ U and GGA+ U study of cerium oxides: Dependence on the effective U parameter, Phys. Rev. B 75 (2007) 035115.
[29] M. Nolan, S.C. Parker, G.W. Watson, The electronic structure of oxygen vacancy defects at the low index surfaces of ceria, Surf. Sci. 595 (2005) 223–232.
[30] N. Skorodumova, S. Simak, B.I. Lundqvist, I. Abrikosov, B. Johansson, Quantum origin of the oxygen storage capability of ceria, Phys. Rev. Lett. 89 (2002) 166601.
[31] M. Cococcioni, S. De Gironcoli, Linear response approach to the calculation of the effective interaction parameters in the LDA+ U method, Phys. Rev. B 71 (2005) 035105.
[32] S. Fabris, G. Vicario, G. Balducci, S. de Gironcoli, S. Baroni, Electronic and atomistic structures of clean and reduced ceria surfaces, J. Phys. Chem. B 109 (2005) 22860–22867.
[33] P. Lott, P. Dolcet, M. Casapu, J.-D. Grunwaldt, O. Deutschmann, The effect of prereduction on the performance of Pd/Al_2O_3 and Pd/CeO_2 catalysts during methane oxidation, Ind. Eng. Chem. Res. 58 (2019) 12561–12570.
[34] D. Jiang, G. Wan, J. Halldin Stenlid, C.E. García-Vargas, J. Zhang, C. Sun, J. Li, F. Abild-Pedersen, C.J. Tassone, Y. Wang, Dynamic and reversible transformations of subnanometre-sized palladium on ceria for efficient methane removal, Nat. Catal. (2023) 1–10.
[35] J. Au-Yeung, K. Chen, A.T. Bell, E. Iglesia, Isotopic studies of methane oxidation pathways on PdO catalysts, J. Catal. 188 (1999) 132–139.
[36] D. Ciuparu, L. Pfefferle, Contributions of lattice oxygen to the overall oxygen balance during methane combustion over PdO-based catalysts, Catal. Today 77 (2002) 167–179.
[37] Y.-Q. Su, J.-X. Liu, I.A.W. Filot, L. Zhang, E.J.M. Hensen, Highly Active and Stable CH4 Oxidation by Substitution of Ce^{4+} by Two Pd^{2+} Ions in CeO_2(111), ACS Catal. 8 (2018) 6552–6559.
[38] A.Y. Stakheev, A.M. Batkin, N.S. Teleguina, G.O. Bragina, V.I. Zaikovsky, I. P. Prosvirin, A.K. Khudorozhkov, V.I. Bukhtiyarov, Particle Size Effect on CH_4 Oxidation Over Noble Metals: Comparison of Pt and Pd Catalysts, Top. Catal. 56 (2013) 306–310.
[39] A. Boubnov, A. Gremminger, M. Casapu, O. Deutschmann, J.D. Grunwaldt, Dynamics of the Reversible Inhibition during Methane Oxidation on Bimetallic Pd-Pt Catalysts Studied by Modulation-Excitation XAS and DRIFTS, ChemCatChem 14 (2022) e202200573.
[40] R. Gholami, M. Alyani, K.J. Smith, Deactivation of Pd Catalysts by Water during Low Temperature Methane Oxidation Relevant to Natural Gas Vehicle Converters, Catalysts 5 (2015) 561–594.
[41] A. Gremminger, J. Pihl, M. Casapu, J.-D. Grunwaldt, T.J. Toops, O. Deutschmann, PGM based catalysts for exhaust-gas after-treatment under typical diesel, gasoline and gas engine conditions with focus on methane and formaldehyde oxidation, Appl. Catal. B 265 (2020) 118571.
[42] J.L. Lu, S. Kaya, J. Weissenrieder, H.J. Gao, S. Shaikhutdinov, H.J. Freund, Low temperature CO induced growth of Pd supported on a monolayer silica film, Surf. Sci. 600 (2006) L153–L157.
[43] G.S. Parkinson, Z. Novotny, G. Argentero, M. Schmid, J. Pavelec, R. Kosak, P. Blaha, U. Diebold, Carbon monoxide-induced adatom sintering in a Pd–Fe_3O_4 model catalyst, Nat. Mat. 12 (2013) 724–728.
[44] Y. Ryou, J. Lee, Y. Kim, S. Hwang, H. Lee, C.H. Kim, D.H. Kim, Effect of reduction treatments (H_2 vs. CO) on the NO adsorption ability and the physicochemical properties of Pd/SSZ-13 passive NO_x adsorber for cold start application, Appl. Catal. A 569 (2019) 28–34.
[45] G. Spezzati, Y. Su, J.P. Hofmann, A.D. Benavidez, A.T. DeLaRiva, J. McCabe, A. K. Datye, E.J. Hensen, Atomically dispersed Pd–O species on CeO_2 (111) as highly active sites for low-temperature CO oxidation, ACS Catal. 7 (2017) 6887–6891.
[46] D. Jiang, G. Wan, C.E. Garcia-Vargas, L. Li, X.I. Pereira-Hernandez, C. Wang, Y. Wang, Elucidation of the active sites in single-atom Pd_1/CeO_2 catalysts for low-temperature CO oxidation, ACS Catal. 10 (2020) 11356–11364.
[47] A. Salcedo, D. Zengel, F. Maurer, M. Casapu, J.D. Grunwaldt, C. Michel, D. Loffreda, Identifying the Structure of Supported Metal Catalysts Using Vibrational Fingerprints from Ab Initio Nanoscale Models, Small (2023) 2300945.
[48] A. Tereshchenko, A. Guda, V. Polyakov, Y. Rusalev, V. Butova, A. Soldatov, Pd nanoparticle growth monitored by DRIFT spectroscopy of adsorbed CO, Analyst 145 (2020) 7534–7540.

[49] P.G. Lustemberg, C. Yang, Y. Wang, C. Wöll, M.V. Ganduglia-Pirovano, Vibrational frequencies of CO bound to all three low-index cerium oxide surfaces: A consistent theoretical description of vacancy-induced changes using density functional theory, J. Chem. Phys. (2023) 159.
[50] A.L. Bugaev, A.A. Guda, K.A. Lomachenko, V.V. Srabionyan, L.A. Bugaev, A. V. Soldatov, C. Lamberti, V.P. Dmitriev, J.A. van Bokhoven, Temperature-and pressure-dependent hydrogen concentration in supported PdH_x nanoparticles by Pd K-edge X-ray absorption spectroscopy, J. Phys. Chem. C. 118 (2014) 10416–10423.
[51] M. Selinsek, B.J. Deschner, D.E. Doronkin, T.L. Sheppard, J.-D. Grunwaldt, R. Dittmeyer, Revealing the structure and mechanism of palladium during direct synthesis of hydrogen peroxide in continuous flow using operando spectroscopy, ACS Catal. 8 (2018) 2546–2557.
[52] M.W. Tew, J.T. Miller, J.A. van Bokhoven, Particle Size Effect of Hydride Formation and Surface Hydrogen Adsorption of Nanosized Palladium Catalysts: L_3 Edge vs K Edge X-ray Absorption Spectroscopy, J. Phys. Chem. C. 113 (2009) 15140–15147.
[53] D. Teschner, J. Borsodi, A. Wootsch, Z. Révay, M. Havecker, A. Knop-Gericke, S. D. Jackson, R. Schlögl, The roles of subsurface carbon and hydrogen in palladium-catalyzed alkyne hydrogenation, Science 320 (2008) 86–89.
[54] M. García-Mota, B. Bridier, J. Pérez-Ramírez, N. López, Interplay between carbon monoxide, hydrides, and carbides in selective alkyne hydrogenation on palladium, J. Catal. 273 (2010) 92–102.
[55] L. Nykänen, J. Andersin, K. Honkala, First-principles calculations of the initial incorporation of carbon into flat and stepped Pd surfaces, Phys. Rev. B 81 (2010) 075417.
[56] S.B. Ziemecki, G.A. Jones, D.G. Swartzfager, R.L. Harlow, J. Faber Jr., Formation of interstitial palladium-carbon phase by interaction of ethylene, acetylene, and carbon monoxide with palladium, JACS 107 (1985) 4547–4548.
[57] M. Maciejewski, A. Baiker, Incorporation of carbon into palladium during low-temperature disproportionation of carbon monoxide over palladium/zirconia prepared from glassy palladium-zirconium, J. Phys. Chem. 98 (1994) 285–290.
[58] D. Teschner, E. Vass, M. Hävecker, S. Zafeiratos, P. Schnörch, H. Sauer, A. Knop-Gericke, R. Schlögl, M. Chamam, A. Wootsch, Alkyne hydrogenation over Pd catalysts: A new paradigm, J. Catal. 242 (2006) 26–37.
[59] A. Hellman, A. Resta, N.M. Martin, J. Gustafson, A. Trinchero, P.A. Carlsson, O. Balmes, R. Felici, R. van Rijn, J.W.M. Frenken, J.N. Andersen, E. Lundgren, H. Grönbeck, The Active Phase of Palladium during Methane Oxidation, J. Phys. Chem. Lett. 3 (2012) 678–682.
[60] Y. Mahara, K. Murata, K. Ueda, J. Ohyama, K. Kato, A. Satsuma, Time Resolved insitu DXAFS Revealing Highly Active Species of PdO Nanoparticle Catalyst for CH_4 Oxidation, ChemCatChem 10 (2018) 3384–3387.
[61] A.K. Datye, J. Bravo, T.R. Nelson, P. Atanasova, M. Lyubovsky, L. Pfefferle, Catalyst microstructure and methane oxidation reactivity during the Pd↔PdO transformation on alumina supports, Appl. Catal. A 198 (2000) 179–196.
[62] T.V. Choudhary, S. Banerjee, V.R. Choudhary, Influence of PdO content and pathway of its formation on methane combustion activity, Catal. Comm. 6 (2005) 97–100.
[63] Y. Cui, J. Zhu Chen, B. Peng, L. Kovarik, A. Devaraj, Z. Li, T. Ma, Y. Wang, J. Szanyi, J.T. Miller, Y. Wang, F. Gao, Onset of High Methane Combustion Rates over Supported Palladium Catalysts: From Isolated Pd Cations to PdO Nanoparticles, JACS Au 1 (2021) 396–408.
[64] A.D. Mayernick, M.J. Janik, Methane oxidation on Pd–Ceria: A DFT study of the mechanism over $Pd_xCe_{1-x}O_2$, Pd, and PdO, J. Catal. 278 (2011) 16–25.
[65] K.-i Fujimoto, F.H. Ribeiro, M. Avalos-Borja, E. Iglesia, Structure and Reactivity of PdO_x/ZrO_2 Catalysts for Methane Oxidation at Low Temperatures, J. Catal. 179 (1998) 431–442.
[66] M. Blanco-Rey, S.J. Jenkins, Methane dissociation and methyl diffusion on PdO {100}, J. Chem. Phys. 130 (2009) 014705.
[67] S. Chen, S. Li, R. You, Z. Guo, F. Wang, G. Li, W. Yuan, B. Zhu, Y. Gao, Z. Zhang, H. Yang, Y. Wang, Elucidation of Active Sites for CH_4 Catalytic Oxidation over Pd/CeO_2 Via Tailoring Metal–Support Interactions, ACS Catal. 11 (2021) 5666–5677.
[68] J. Nilsson, P.-A. Carlsson, S. Fouladvand, N.M. Martin, J. Gustafson, M.A. Newton, E. Lundgren, H. Grönbeck, M. Skoglundh, Chemistry of Supported Palladium Nanoparticles during Methane Oxidation, ACS Catal. 5 (2015) 2481–2489.
[69] G. Ferré, M. Aouine, F. Bosselet, L. Burel, F.C.S. Aires, C. Geantet, S. Ntais, F. Maurer, M. Casapu, J.-D. Grunwaldt, Exploiting the dynamic properties of Pt on ceria for low-temperature CO oxidation, Catal. Sci. Technol. 10 (2020) 3904–3917.
[70] Z. Wu, M. Li, J. Howe, H.M. Meyer III, S.H. Overbury, Probing defect sites on CeO_2 nanocrystals with well-defined surface planes by Raman spectroscopy and O_2 adsorption, Langmuir 26 (2010) 16595–16606.
[71] G.W. Graham, A.E. O'Neill, D. Uy, W.H. Weber, H. Sun, X.Q. Pan, Observation of strained PdO in an aged Pd/ceria-zirconia catalyst, Catal. Lett. 79 (2002) 99–105.
[72] S. Loridant, Raman spectroscopy as a powerful tool to characterize ceria-based catalysts, Catal. Today 373 (2021) 98–111.
[73] R. Gulyaev, T.Y. Kardash, S. Malykhin, O. Stonkus, A. Ivanova, A. Boronin, The local structure of $Pd_xCe_{1-x}O_{2-x-\delta}$ solid solutions, PCCP 16 (2014) 13523–13539.